A FINITE DIFFERENCE TIME DOMAIN STUDY ON THE DESIGN OF

MICROWAVE CATHETERS

A Thesis

by

MOHAMMAD MAZEN MOHAMMAD AL-KHALDI

Submitted to the Office of Graduate and Professional Studies of
Texas A&M University
in partial fulfillment of the requirements for the degree of

MASTER OF SCIENCE

Chair of Committee,	Kai Chang
Co-Chair of Committee,	Robert D. Nevels
Committee Members,	Steven M. Wright
	Chin B. Su
Head of Department,	Miroslav M. Begovic

August 2017

Major Subject: Electrical Engineering

ABSTRACT

An investigation of the design aspects along with proposed improvements in the construction of microwave ablation catheters are reported in this thesis. The computational methods used to carry out this research include an in-house created cylindrical coordinate rotationally symmetric Finite Difference Time Domain (FDTD) scheme.

Firstly, a systematic means of modelling and designing microwave catheters is proposed. The method capitalizes on the rotationally symmetric nature of the microwave catheter and reduces the design from three dimensions to a two-dimensional problem.

Secondly issues related to resonant frequency and leaky waves, an inherent property of microwave ablation, are investigated and subsequent solutions are proposed. For the issue of resonant frequency, the addition of a terminating cap halves the catheter's resonant frequency allowing for acceptable return loss, less than -10 dB, at a resonant frequency of 2.7 GHz without a sleeve choke and 2.45 GHz with a choke.

Several designs are investigated in order to eliminate the power coupled into waves travelling along the coaxial feedline's exterior. The proposed catheter design with the sleeve choke is successful at eliminating surface waves whilst attaining a return loss of -14.61 dB at resonance. The internally matched catheter is equally as effective and attains a return loss of -49.39 dB at resonance while the catheter with a floating sleeve only partially reduces the amplitude of surface waves whilst achieving a return

loss of -39.08 dB at resonance. The effectiveness of adding a dielectric cylinder around the monopole in order to improve return loss, bandwidth and overall Specific Absorption Rate (SAR) distribution is also investigated.

Near to far field transformations are implemented and the far field pattern of the catheter is shown to be that of a dipole, at resonance. Furthermore, a dispersive FDTD algorithm is developed to incorporate a metamaterial plug. The effects of this are shown to be highly dependent on the dielectric properties of the metamaterial and act to lower the resonant frequency allowing for overall length reductions. Finally, the bioheat equation is investigated and is implemented in the context of microwave catheters by analyzing temperature rise at varying radial distances from the catheter.

DEDICATION

To the loving memory of my late grandparents, my parents and siblings

ACKNOWLEDGEMENTS

First, I thank the all mighty for his guidance and divine providence. Without his countless blessings, none of this would have been possible. This thesis appears in its current form due to the patience, guidance and wisdom of a number of people to whom I would like to extend my sincere gratitude.

To Dr. Robert Nevels, I extend my sincere gratitude and deep indebtedness for his kindness, support and wisdom. His feedback has made me a better researcher and engineer. To Dr. Kai Chang, I extend my deep appreciation and gratefulness for his continued support, guidance and patience. Further, my deep gratitude and sincere appreciation goes to Dr. Steven Wright for all his help, patience and support. I also thank Dr. Chin Su for his time, encouragement, advice and support. To Dr. Jose Silva-Martinez, I extend my gratitude for his inestimable advice and patience as well as that of the administrative staff at the Department of Electrical and Computer Engineering at Texas A&M University.

My sincere gratitude and appreciation goes to my family for their unyielding support, continued sacrifice and never ending love. Without them, this work would not have been possible.

Finally, I would like to thank my friends at the American University of Sharjah Omar Ghazal, Abdalqader Altawil and Omar Khatib for their moral support as well as my friends here at Texas A&M University Hasan Abbas, Jongchul Shin, Hussain Ibdah and Dr. Muneer to name a few.

CONTRIBUTORS AND FUNDING SOURCES

Contributors

This work was supervised by a thesis committee consisting of Professor Robert Nevels and Professor Kai Chang as co-advisors as well as Professors Steven Wright and Chin Su as committee members, of the Electrical and Computer Engineering Department.

Funding Sources

NOMENCLATURE

ABC	Absorbing Boundary Condition
DFT	Discrete Fourier Transform
DNG	Double Negative
E-field	Electric Field
ENG	Epsilon Negative
FDTD	Finite Difference Time Domain
LHM	Left Handed Material
MoM	Method of Moments
MW	Microwave
PML	Perfectly Matched Layer
RL	Return Loss
RF	Radio Frequency
SAR	Specific Absorption Rate
UPML	Uniaxial Perfectly Matched Layer
WHO	World Health Organization
VSWR	Voltage Standing Wave Ratio

TABLE OF CONTENTS

LIST OF FIGURES

LIST OF TABLES

CHAPTER I

INTRODUCTION

While originally, surgical and largely invasive means were employed for the

purpose of annihilating aberrant tissue and growths it is catheters that are now being

used to address this issue. Catheters assume three primary variants which include high

energy DC-induced current cauterization, radio frequency (RF) methods and the method

of interest, ablation using the microwave (MW) catheter. All three of the

aforementioned techniques entail catheter probes that are inserted through a vein, usually

in the arm or leg, and navigated through until they reach the heart where ablation takes

place. It is worth mentioning that the proposed designs in this thesis were primarily

intended for use in heart ablation procedures, but their usefulness can be generalized to

application in various organs within the body that may require ablation. Both DC and

RF ablation procedures require that physical contact be made with the aberrant tissue in

order to allow for the flow of current from the tip of the catheter to the affected tissue,

thereby acting as conductors and not radiators. These two methods also require that a

plate be placed on the chest which together with the catheters acts as an electrode. This

allows the ablated area to be spread rather than be highly concentrated on the tip of the

catheters.   However, one of the numerous advantages of MW ablation is that it renders

physical contact between the metal surface of the probe and the tissue unnecessary and

delivers the desired effect exclusively through radiation from the Teflon coated catheter

microwave probe.

1.1. Motivation

Microwave catheters are becoming, slowly but surely, more attractive in their use for ablation and treatment purposes. Initially, in order to address any aberrancies in tissues surgical means were used, where if the aberrant tissue was in the patient's heart this would have involved open heart surgery and conducting what is commonly referred to as a Maze procedure. However, breakthroughs rendered these techniques as obsolete and now employ catheters to address such issues. Microwave ablation has been experimentally proven to offer several advantages over its counterparts including its reduced susceptibility to heat sink effects, more versatility, greater heat deposition depth without destroying tissue and maneuverability. It is also associated with the elimination of some of the known effects related to ablation including ventricle fibrillation, arrhythmia as well as involuntary motion associated with increasingly large current densities.

In practical application, MW ablation has seen limited commercial adoption. This can be owed to the limited designs put forth, many of which suffer from deficiencies pertaining to their return loss and/or SAR distribution that render them unusable with patients. This thesis will attempt to propose a systematic means through which MW catheters can be designed, identify the deficiencies that may be associated with existing designs and propose means to mitigate them.

1.2. Thesis Outline

Taking into account that the bulk of the numerical analysis presented in this thesis employs Finite Difference Time Domain (FDTD) numerical analysis, its general foundations and relevant formulation will be discussed and will then proceed to outlining its relevance to the issue of microwave catheter design. This will include a comprehensive discussion of fundamental formulation and parameters of interest associated with FDTD modelling. It will then proceed to discussing the most pertinent considerations associated with the proposed catheter designs, namely return loss and Specific Absorption Rate (SAR). Next, a comparative study will be conducted aimed at analyzing various means of improving SAR distribution and the effect SAR has on return loss. Next is a method that employs near-to-far-field transformations in the context of microwave catheters in order to obtain the catheter's radiation pattern.

The next chapter will discuss design aspects associated with FDTD modelling of metamaterials. This will be complemented with a discussion on dispersive FDTD. This chapter would end with an analysis of the effects of using metamaterials in the context of microwave catheters in the form of a metamaterial plug. Its impact on SAR, return loss and bandwidth will be analyzed.

This will be followed by a discussion on the bioheat equation. The numerical fundamentals and potential applications will be discussed and the relevant FDTD formulation in a cylindrical coordinate system will be proposed. FDTD applications in the context of microwave catheters will be discussed and the relevant findings will be put forth.

In conclusion, a summary will be provided offering an overview of the most important highlights of this research and recommendations for future work.

CHAPTER II

BACKGROUND

2.1.   Brief Historical Overview

While significant work has been done on numerical methods in general, and

frequency domain integral equation based solutions of Maxwell's equations in particular,

it was during the time period between 1970 to 1980 that their inherent limitations were

realized. This prompted academic institutions as well as defense agencies to explore

alternative means of conducting electromagnetic analysis numerically. These efforts led

to the rise of time domain differential equation solutions of Maxwell's equations and

their initial formulation can be credited to Kane Yee. Their wide scale adoption and

application was not until the 1990's onwards when it was coined the Finite Difference

Time Domain (FDTD). Interest in this particular numerical method can be credited to its

numerous advantages; those are as follows: taking into account the fact that it is a fully

explicit solution of Maxwell's equations, it employs no linear algebra and therefore it

reduces limitations on the size of electromagnetic models. Theoretically there exists no

upper bound on field unknowns, though practically this is roughly 10^9 whilst under the

same memory constraints frequency domain integral equation methods are limited to less

than 10^6 unknowns. Furthermore, while the FDTD method may not be the most accurate

numerical method for the analysis of electromagnetic systems, its sources of errors are

well understood and within the error margins of interest, can be mitigated. Therefore, it

is one of the few usable methods that offer an acceptable compromise between accuracy,

simplicity and robustness. Further, concerning the issue of simplicity, the FDTD method

does not employ structure dependent Green's functions and therefore does not require

overhauling of formulation every time the structure of interest is changed. Moreover, it

allows for extensive visualization of related simulation results, a capability of profound

implications. This allows one to visualize field propagation and a slew of electric

quantities in general, and electromagnetic quantities in particular [1]. It is because of its

vast array of advantages that the numbers of papers published with relevance to the

FDTD method grew by a margin of more than 3000 % by 1995 compared to the year

1985 [2].

2.2.   *Maxwell's Equations*

At the foundation of all electromagnetic analysis is the set of Maxwell's

equations. They are partial differential equations which describe the generation,

propagation and effects of electric and magnetic fields brought about by the presence of

charge and thereof its motion. They assume the following forms:

$$\frac{\partial \vec{B}}{\partial t} = -\nabla \times \vec{E} - \vec{M} \tag{2.1}$$

$$\frac{\partial \vec{D}}{\partial t} = \nabla \times \vec{H} - \vec{J} \tag{2.2}$$

$$\nabla \cdot \vec{D} = \rho_e \tag{2.3}$$

$$\nabla \cdot \vec{B} = \rho_m \tag{2.4}$$

$\vec{E}$: Electric field intensity (V/m)

$\vec{H}$: Magnetic field intensity (A/m)

$\vec{D}$: Electric flux density (C/m^2)

$\vec{B}$: Magnetic flux density (Wb/m^2)

$\vec{J}$: Electric current density (A/m^2)

$\vec{M}$: Magnetic current density (V/m^2)

ρ_e : Electric charge density (A/m^3)

ρ_m : Magnetic charge density (V/m^3)

      When investigating electromagnetic phenomena, it is almost always the case that a set of coupled differential equations ought to be solved. It is therefore necessary to establish relations between the electric field intensity and its corresponding electric flux density as well as a relationship between the magnetic field intensity and the magnetic flux density. In homogeneous media, the relationship is most accessibly defined through a set of constitutive relations. These assume the following form:

$$\vec{D} = \varepsilon\vec{E} = \varepsilon_r\varepsilon_0\vec{E} \tag{2.5}$$

$$\vec{B} = \mu\vec{H} = \mu_r\mu_0\vec{H} \tag{2.6}$$

ε : Electric permittivity (F/m)

ε_r : Relative permittivity

ε_0 : Free space permittivity

μ : Magnetic permeability (H/m)

μ_r : Relative permeability

μ_0 : Free space permeability

However, in realistic mimicking of real life scenarios; the media of interest may not be accurately represented as a homogenous medium. A linear, isotropic and nondispersive response may not necessarily be the case. In such a scenario, relationships similar to (2.5) and (2.6) may be established through an empirical or theoretical approach. Inhomogeneity can arise from three main factors which include dispersion, nonlinearity and anisotropy. Dispersive media will generally have to satisfy one or both conditions of ε and μ being functions of frequency. On the other hand, nonlinearity occurs when ε and μ behave as functions of field intensities. Finally, anisotropy refers to the situation where ε and μ are tensors. This occurs in material that exhibits either birefringence or dichroism where the medium will have a refractive index which is dependent on polarization or will absorb incident waves at different rates depending on their polarization [3].

Ultimately, in a homogeneous source free region the Maxwell curl equations are given by (2.7) and (2.8) shown below.

$$\frac{\partial \vec{E}}{\partial t} = \frac{1}{\varepsilon} \nabla \times \vec{H} \tag{2.7}$$

$$\frac{\partial \vec{H}}{\partial t} = -\frac{1}{\mu} \nabla \times \vec{E} \tag{2.8}$$

A further step which would get one closer to the practical implementation of this set of equations is expressing the vector components of the curl operators as a system of coupled scalar equations given by (2.9 - 2.14).

$$\frac{\partial E_x}{\partial t} = \frac{1}{\varepsilon}\left[\frac{\partial H_z}{\partial y} - \frac{\partial H_y}{\partial z}\right] \tag{2.9}$$

$$\frac{\partial E_y}{\partial t} = \frac{1}{\varepsilon}\left[\frac{\partial H_x}{\partial z} - \frac{\partial H_z}{\partial x}\right] \tag{2.10}$$

$$\frac{\partial E_z}{\partial t} = \frac{1}{\varepsilon}\left[\frac{\partial H_y}{\partial x} - \frac{\partial H_x}{\partial y}\right] \tag{2.11}$$

$$\frac{\partial H_x}{\partial t} = \frac{1}{\mu}\left[\frac{\partial E_y}{\partial z} - \frac{\partial E_z}{\partial y}\right] \tag{2.12}$$

$$\frac{\partial H_y}{\partial t} = \frac{1}{\mu}\left[\frac{\partial E_z}{\partial x} - \frac{\partial E_x}{\partial z}\right] \tag{2.13}$$

$$\frac{\partial H_z}{\partial t} = \frac{1}{\mu}\left[\frac{\partial E_x}{\partial y} - \frac{\partial E_y}{\partial x}\right] \tag{2.14}$$

For a large array of applications two dimensional simulations suffice. Furthermore, in non-Cartesian co-ordinate systems complex structures may also be analyzed using a two dimensional FDTD algorithm through exploiting a structures' axial symmetry. It is therefore particularly useful to reduce the set of coupled scalar equations listed in the preceding section to two dimensions.

Consider a situation in which the structure of interest extends to infinity in the z-direction. Further, all incident waves are uniform in the same direction. Under such conditions, variation in the z-direction is nonexistent causing all partial derivatives with respect to the z-direction to be zero. This reduces the preceding set of equations to the following:

$$\frac{\partial E_x}{\partial t} = \frac{1}{\varepsilon} \frac{\partial H_z}{\partial y} \tag{2.15}$$

$$\frac{\partial E_y}{\partial t} = -\frac{1}{\varepsilon} \frac{\partial H_z}{\partial x} \tag{2.16}$$

$$\frac{\partial E_z}{\partial t} = \frac{1}{\varepsilon} \frac{\partial H_y}{\partial x} \tag{2.17}$$

$$\frac{\partial H_x}{\partial t} = -\frac{1}{\mu} \frac{\partial E_z}{\partial y} \tag{2.18}$$

$$\frac{\partial H_z}{\partial t} = \frac{1}{\mu} \frac{\partial E_x}{\partial y} \tag{2.19}$$

Here, it becomes necessary to make a distinction between TM and TE modes. The set of equations for the TM mode are given by (2.20 - 2.22) where their counterparts for the TE$_z$ mode are given by (2.23 - 2.25).

$$\frac{\partial E_z}{\partial t} = \frac{1}{\varepsilon} \left[\frac{\partial H_y}{\partial x} - \frac{\partial H_x}{\partial y} \right] \tag{2.20}$$

$$\frac{\partial H_x}{\partial t} = -\frac{1}{\mu} \frac{\partial E_z}{\partial y} \tag{2.21}$$

$$\frac{\partial H_y}{\partial t} = \frac{1}{\mu} \frac{\partial E_z}{\partial x} \tag{2.22}$$

$$\frac{\partial E_x}{\partial t} = \frac{1}{\varepsilon} \frac{\partial H_z}{\partial y} \tag{2.23}$$

$$\frac{\partial E_y}{\partial t} = -\frac{1}{\varepsilon} \frac{\partial H_z}{\partial x} \tag{2.24}$$

$$\frac{\partial H_z}{\partial t} = \frac{1}{\mu} \left[\frac{\partial E_x}{\partial y} - \frac{\partial E_y}{\partial x} \right] \tag{2.25}$$

10

Note, that the two modes share no common field components allowing for their simultaneous existence without running the risk of interaction. The two dissimilar modes represent two approaches through which electromagnetic simulations can be undertaken. Here, insight into boundary conditions and the nature of the structure is of paramount importance. Consider the TE case as an example. In its formulation, the electric field is set up such that it is in a plane perpendicular to the z-axis. In a scenario where the structure of interest is metallic, the electric field can be supported in the vicinity of the metallic structure in a perpendicular or adjacent orientation whilst maintaining zero tangential electric field condition on the surface of the metal. In contrast, whilst implementing the relevant formulation for the TM mode the electric field lines can only be parallel to the z-axis. Therefore, it is of grave importance to have the application and structure in mind before pursuing the formulation of the relevant FDTD analysis.

2.3. Yee Algorithm

As mentioned earlier, it was Yee who first introduced the method through which a set of finite difference equations for Maxwell's equations which are time dependent can be used to solve for both the electric and magnetic fields in time and space by employing the coupled curl equations [4]. The idea is illustrated in Fig. 1 in a three dimensional lattice where every electric field component is surrounded by four circulating magnetic field components.

11
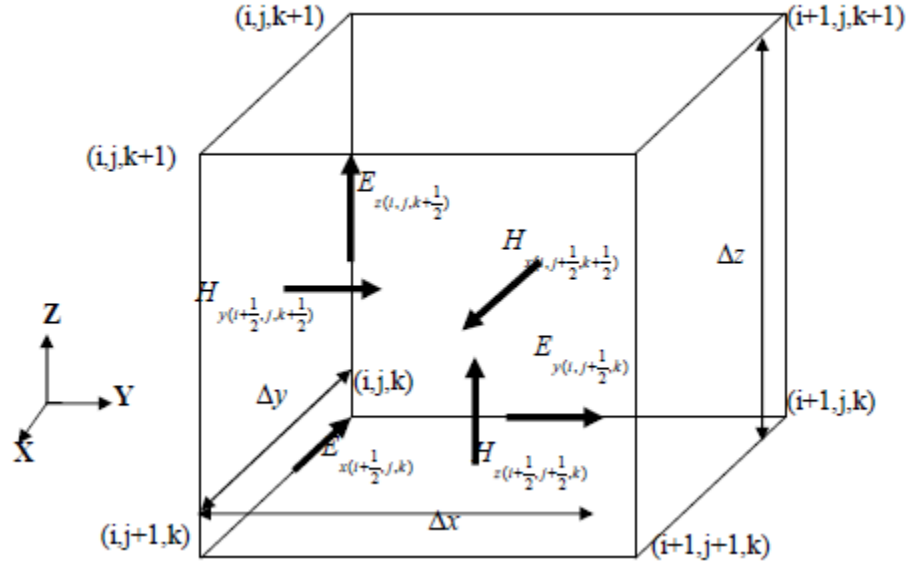
Fig. 1. Position of electric and magnetic fields on the Yee lattice

This offers numerous advantages as it is analogous to combined field integral equations employed by MoM. Furthermore, the combined computation of electric and magnetic fields allows for a more accurate and robust representation of electromagnetic phenomenon associated with various structures of interest. Moreover, it would also allow for the implementation of specialized approaches aimed at addressing singularities associated with edges, corners, thin wire approximations and points near singularities. In Yee's algorithm, what is known as a leapfrog arrangement is employed. In this arrangement, a fully explicit solution is used thereby mitigating the need to address simultaneous equations and corresponding matrix inversions. The algorithm employs a second order accurate central difference theorem.

Here it is important to point out that for all subsequent formulation, the following notation is employed $(i, j, k) = (i\Delta x, j\Delta y, k\Delta z)$ in which Δx, Δy and Δz represent spatial increments in the x, y and z direction whilst i, j and k are integers. In addition, Δt will represent the increment in time.

There exists two sets of update equations, each corresponding to the TM and TE modes respectively. The later will be of interest which contains two electric field components and one magnetic field component, synonymous with the TM case which will be used when conversion to cylindrical coordinates takes place.

$$E_x\Big|_{i,j+1/2}^{n+1/2} = C_a(m) E_x\Big|_{i,j+1/2}^{n-1/2} + C_b(m)\left(H_z\Big|_{i,j+1}^{n} - H_z\Big|_{i,j}^{n}\right) \tag{2.26}$$

$$E_y\Big|_{i-1/2,j+1}^{n+1/2} = C_a(m) E_y\Big|_{i-1/2,j+1}^{n-1/2} + C_b(m)\left(H_z\Big|_{i-1,j+1}^{n} - H_z\Big|_{i,j+1}^{n}\right) \tag{2.27}$$

$$H_z\Big|_{i,j+1}^{n+1} = D_a(m) H_z\Big|_{i,j+1}^{n} + D_b(m)\begin{bmatrix}\left(E_x\Big|_{i,j+3/2}^{n+1/2} - E_x\Big|_{i,j+1/2}^{n+1/2}\right) \\ -\left(E_y\Big|_{i+1/2,j+1}^{n+1/2} - E_y\Big|_{i-1/2,j+1}^{n+1/2}\right)\end{bmatrix} \tag{2.28}$$

$$C_a\Big|_{i,j,k} = \left(1 - \frac{\sigma_{i,j,k}\Delta t}{2\varepsilon_{i,j,k}}\right)\Bigg/\left(1 + \frac{\sigma_{i,j,k}\Delta t}{2\varepsilon_{i,j,k}}\right) \tag{2.29}$$

$$C_b\Big|_{i,j,k} = \left(\frac{\Delta t}{\varepsilon_{i,j,k}\Delta}\right)\Bigg/\left(1 + \frac{\sigma_{i,j,k}\Delta t}{2\varepsilon_{i,j,k}}\right) \tag{2.30}$$

$$D_a\Big|_{i,j,k} = \left(1 - \frac{\sigma_{i,j,k}^*\Delta t}{2\mu_{i,j,k}}\right)\Bigg/\left(1 + \frac{\sigma_{i,j,k}^*\Delta t}{2\mu_{i,j,k}}\right) \tag{2.31}$$

13

$$D_b\big|_{i,j,k} = \left(\frac{\Delta t}{\mu_{i,j,k}\Delta}\right) \Bigg/ \left(1 + \frac{\sigma^*_{i,j,k}\Delta t}{2\mu_{i,j,k}}\right) \tag{2.32}$$

The Yee algorithm requires that special attention be paid to numerical dispersion, computational stability and absorption of outgoing waves at the numerical boundary. Discussions concerning these phenomena has been well documented in the relevant literature and will not be covered here.

2.4.   *Source Excitation*

In this section, the fundamental concepts underlying introducing an electromagnetic source field into the numerical space are discussed. Here we will employ a soft source in which the virtual source will allow reflected numerical waves to pass through the point of excitation without hindrance. This can be illustrated using the one-dimensional TM case as shown below:

$$\nabla \times \overrightarrow{H} = \varepsilon_0 \frac{\partial \overrightarrow{E}}{\partial t} + \overrightarrow{J} \tag{2.33}$$

$$\frac{\partial E_z}{\partial t} = \frac{1}{\varepsilon_0}\frac{\partial H_y}{\partial x} - \frac{J_z}{\varepsilon_0} \tag{2.34}$$

By assuming that excitation current density is zero everywhere except for the source point, the Yee update equations can be modified to assume the following forms:

$$E_z\big|_{i_s}^{n+1} = E_z\big|_{i_s}^{n} + \frac{\Delta t}{\varepsilon_0 \Delta x}\left(H_y\big|_{i_s+1/2}^{n+1/2} - H_y\big|_{i_s-1/2}^{n+1/2}\right) - \frac{J_z\big|_{i_s}^{n+1/2}}{\varepsilon_0} \tag{2.35}$$

14

$$E_z\Big|_{i_s}^{n+1} = E_z\Big|_{i_s}^{n} + \frac{\Delta t}{\varepsilon_0 \Delta x}\left(H_y\Big|_{i_s+1/2}^{n+1/2} - H_y\Big|_{i_s-1/2}^{n+1/2}\right) + E_{source}\Big|^{n+1/2} \tag{2.36}$$

where the last term denotes the excitation waveform of interest.

There exists a wide range of possible waveforms which can act as excitations. The most popular of which is the Gaussian pulse. This assumes the form in (2.37).

$$g(n\Delta t) = e^{\frac{-(n\Delta t - n_0 \Delta t)^2}{(\beta \Delta t)^2}} \tag{2.37}$$

as a general rule of thumb, n_0 should be chosen such that at time $n=0$ the function should be down ~140 dB.

Other possible excitations include a ramped sinusoidal function which assumes the following form:

$$g(n\Delta t) = e^{\frac{-(n\Delta t - n_0 \Delta t)^2}{(\beta \Delta t)^2}} \sin\left[2\pi f_0 (n - n_0)\Delta t\right] \tag{2.38}$$

where this particular waveform is centered about n_0. In order to ensure proper transition from zero valued response into the Gaussian pulse n_0 should be at least 4β. The relevant waveforms are depicted in Figs. 2 and 3.
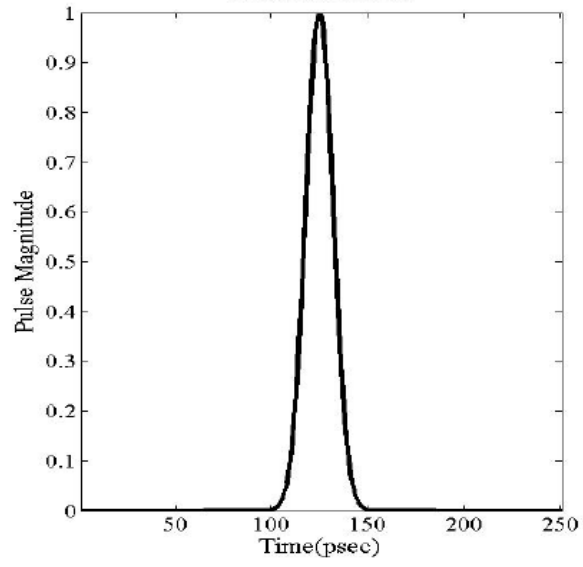
15

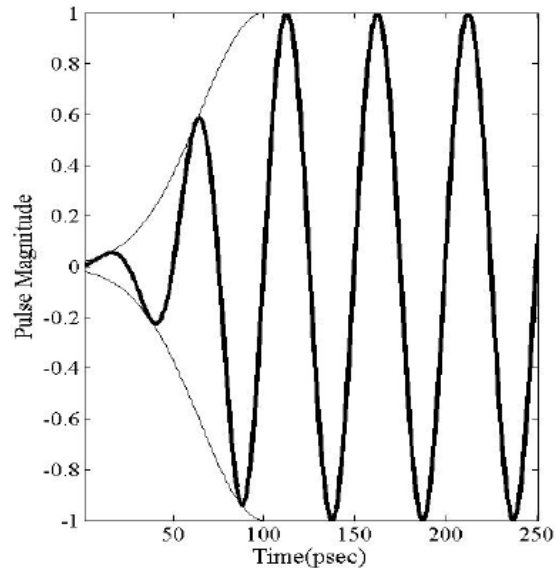Fig. 2. Gaussian pulse excitation

Fig. 3. Ramped sinusoidal excitation

2.5. *Liao Absorbing Boundary Condition*

In this research, the Liao ABC will be employed. Introduced by Liao et al. this absorbing boundary condition relates to extrapolation in both space and time through the use of Newton backward-difference polynomial. It is well established that absorbing boundary conditions cannot be directly obtained from Maxwell's curl equations due to the application of the central difference theorem for their discretization. Taking into account that that application requires the preexisting knowledge of the fields in one half space cell at every side of the observing point it becomes evident why the ABC cannot be directly obtained from Maxwell's curl equations as no information relating to the fields is available at separations equal to or exceeding one half space into the boundary. For this reason extrapolation is necessary and Newton backward-difference polynomial has proven instrumental in implementing a highly effective ABC. Consider the following formulation for the field in a set of space and time points.

$$E_1 = E(t, \text{x}) \tag{2.39}$$

$$E_2 = E(t - \Delta t, x - \Delta x) \tag{2.40}$$

$$E_3 = E(t - 2\Delta t, x - 2\Delta x) \tag{2.41}$$

$$E_N = E(t - N\Delta t, x - N\Delta x) \tag{2.42}$$

Applying the backwards difference operator we get:

$$\Delta^1 E(t, x) = \Delta^1 E_1 = E_1 - E_2 = E(\text{t}, x) - E(t - \Delta t, x - \Delta x) \tag{2.43}$$

$$\Delta^2 E_1 = \Delta^1 E_1 - \Delta^1 E_2 = E(\text{t}, x) - 2E(t - \Delta t, x - \Delta x) + E(t - 2\Delta t, x - 2\Delta x) \tag{2.44}$$

17

$$\Delta^N E(\mathrm{t},x) = \sum_{j=1}^{N+1} (-1)^{j+1} C_{j-1}^N E\left[t-(j-1)\Delta t, x-(j-1)\Delta x\right] \qquad (2.45)$$

$$C_k^N = \frac{N!}{(N-k)!k!} \qquad (2.46)$$

where the application of Newton's backwards difference polynomial for space and time relies on the knowledge of the electric field at a given point x at a previous time step. Newton's backwards difference polynomial for space and time assumes the following form:

$$E\left(t+\beta\Delta t, x_o + \beta\Delta x\right) = E_1 + \beta\Delta^1 E_1 + \frac{\beta(\beta+1)}{2!}\Delta^2 E_1 + \frac{\beta(\beta+1)(\beta+2)}{3!}\Delta^3 E_1 \cdots \qquad (2.47)$$
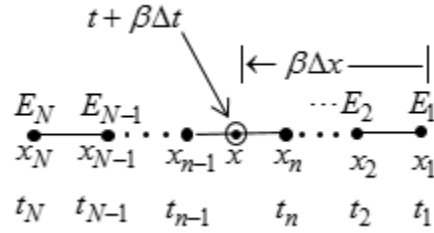
Fig. 4. Interpolation of electric field at boundary

The use of Newton's backward difference polynomial relies on the interpolation of known values of the electric field to find field values at boundary x as depicted in Fig. 4. This adheres to the restriction of $-(N-1) \leq \beta \leq 0$. According to this formula the value of the electric field at point x can only be found at a previous time $(t+\beta\Delta t)$ because each successive E_n has been recorded at a corresponding successive time. Therefore, we

18

would relax the requirement $-(N-1) \leq \beta \leq 0$ by setting $\beta = 1$ allowing for the computation of the electric field values at the boundary x_0 as shown in Fig. 5.
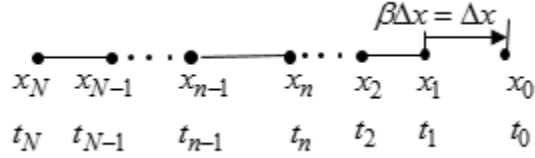

Fig. 5. Effect of relaxing condition and setting $\beta = 1$

We would then be able to solve for the electric field E_0 at the boundary point x_0.

$$E_o = E(x_0,t_0) = E_1 + \Delta^1 E_1 + \Delta^2 E_1 + \cdots \Delta^{N-1} E_1$$
$$= \sum_{j=1}^{N} (-1)^{j+1} C_j^N E\left[t_1 - (j-1)\Delta t, x_1 - (j-1)\Delta x \right], \tag{2.48}$$
$$C_j^N = \frac{N!}{(N-j)!\, j!}$$

CHAPTER III

MICROWAVE CATHETER DESIGN

While originally, surgical and largely invasive means were employed for the purpose of annihilating aberrant tissue and growths it is catheters that are now being used to address this issue. Catheters assume three primary variants which include high energy DC-induced current cauterization, radio frequency (RF) methods and the method of interest, the microwave (MW) method. All three of the aforementioned techniques entail catheter probes that are inserted through a vein, usually in the arm or leg, and navigated through until it reaches the heart where ablation takes place. It is worth mentioning that the proposed designs in this chapter were primarily intended for use in heart ablation procedures, but its usefulness can be generalized to application to various organs within the body that require ablation. Both DC and RF ablation procedures require that physical contact be made with the aberrant tissue in order to allow for the flow of current from the tip of the catheter to an electrode pad placed on the skin's surface. However, one of the numerous advantages of MW ablation is that it renders physical contact to be unnecessary and delivers the desired effect exclusively through heat brought about by microwave radiation from the catheter. Subsequent sections of this chapter will attempt to provide an overview of microwave catheter design and discuss the relevant designs and results.

3.1.   Overview of Microwave Tissue Ablation

The basic goal underlying microwave ablation is to deliver enough power, through radiation, to the affected tissue without causing harm to the patient. The power should be absorbed by the tissue resulting in temperature rise. With sufficient heating the aberrant tissue will wither and turn into scar tissue. The extent of heating and the ablation time are both a function of the severity of the case at hand.

An effective microwave ablation system will need to possess several characteristics. To begin with, it ought to be able to create thermal lesions large enough to span the affected areas and deep enough to cauterize the aberrant tissue completely whilst leaving healthy tissue unaffected. Simultaneously, it will need to overcome heat sink effects associated with blood flow [4]. It is worth mentioning that this effect refers to the cooling consequence blood flow has whereby a portion of the heat produced by the catheter is carried away thus reducing the effectiveness of the ablation procedure. Furthermore, from a practical standpoint the ablation procedure needs to be relatively short in terms of duration. Meeting these conditions will require the use of a compact and highly maneuverable MW catheter.

Microwave ablation is able to provide several advantages over radio frequency ablation, but it is not without drawbacks and deficiencies. Amongst its advantages is the ability to heat tissue at higher temperatures and penetrate further into the aberrant tissue. It has also been reported that MW ablation is less dependent on thermal conduction coefficients of the related tissue as charring is not a common consequence of MW ablation. In addition, its compactness allows for a more robust procedure particularly

with the elimination of a grounding pad. Several catheters can also be employed simultaneously without running the risk of interference. However, its drawbacks include the presence of unwanted backward heating caused by the presence of leaky wave propagation on the periphery of the catheter and on the conductive surfaces within its Teflon coating; an issue which the proposed structures in this thesis will attempt to address. Moreover, the larger the aberrant tissue the less effective MW ablation is likely to be [5]. Furthermore, all dielectric properties of tissue are a function of temperature. The extent of changes in those properties varies as a function of input power and frequency. Other changes include loss in water content due to high temperatures as well as protein de-neutralization. Such changes are typically unaccounted for in numerical modeling. At times this is acceptable depending on ablation duration, input power as well as frequency.

3.2.   *Electromagnetic Interactions in Biological Matter*

As mentioned earlier the success of microwave ablation hinges on its ability to radiate enough energy into the aberrant tissue in order kill the aberrant tissue. Temperature rises within the tissue stem from the induction of potential which leads to the flow of current. Therefore, the impact of an electromagnetic field within the tissue can be categorized under two major effects, the first of which is non-thermal and the second is thermal.

Nonthermal effects refer to the stimulation of the nervous system as well as muscle contraction brought about the flow of current due to the fields radiated from the catheter. Ventricle fibrillation as well as involuntary motion are known effects. In general, these effects will be largely dependent on frequency as well as current density and are factors worth consideration in the DC and RF regime but are inconsequential in the MW regime. Stimulation effects are inversely proportional to frequency [6]. On the other hand, thermal effects relate to a scenario in which the heat caused by the generation of current flow exceeds the body's ability to dissipate heat. A common means of quantizing this effect is through the Specific Absorption Rate (SAR), a term providing a measure of the amount of RF and MW power that is absorbed by biological matter. It is given as:

$$SAR = \frac{\sigma}{\rho}|E|^2 \qquad (3.1)$$

SAR : Specific Absorption Rate (W/kg)

σ : Tissue conductivity (S/m)

ρ : Mass density (kg/m^3)

The World Health Organization (WHO) in [7] tabulated the effects of current flow in tissue and their findings are shown below:

Table 1 - Biological Effects of Various Current Densities

Current Density (mA/m^2)	Effects
<1	No observable effects
1 - 10	Minute effects observed
10 - 100	Several possible effects including magnetophosphene and stimulus of nervous system
100 - 1000	High likelihood of exciting the nervous system
1000 >	Atrial fibrillation and extrasystoles highly probable

3.3.   FDTD in Cylindrical Co-ordinates

Practical modelling of the catheter entails attempting to simplify the problem as much as possible. While at the surface, the use of FDTD in cylindrical co-ordinate systems may seem counterproductive in the attempt to simplify the problem at hand, it turns out to be instrumental in doing so. Taking into account the catheter's rotationally symmetric nature one can follow a procedure similar to that proposed in [8] to model coaxial transmission lines and antennas. The solution departs from expressing Maxwell's equations in cylindrical co-ordinates and the application of the central difference theorem thereof. The modelling will only be concerned with the excitation of the rotationally symmetric TM modes. The relevant formulation is shown below.

$$\frac{\partial E_\rho}{\partial z} - \frac{\partial E_z}{\partial \rho} = -\mu_0 \frac{\partial H_\phi}{\partial t} \qquad (3.2)$$

$$-\frac{\partial H_\phi}{\partial z} = \varepsilon_0 \frac{\partial E_\rho}{\partial t} \qquad (3.3)$$

$$\frac{1}{\rho} \frac{\partial (\rho H_\phi)}{\partial \rho} = \varepsilon_0 \frac{\partial E_z}{\partial t} \qquad (3.4)$$

$$E_\rho^{n+1}(i, j-1/2) = E_\rho^n(i, j-1/2) - \frac{\Delta t}{\varepsilon_0 \Delta z} \left[H_\phi^{n+1/2}(i, j) - H_\phi^{n+1/2}(i, j-1) \right] \qquad (3.5)$$

$$E_z^{n+1}(i+1/2, j) = E_z^n(i+1/2, j) - \frac{\Delta t}{\varepsilon_0 \Delta \rho} \frac{1}{\rho_{i+1/2}} \left[\begin{array}{c} \rho_{i+1/2} H_\phi^{n+1/2}(i+1, j) \\ -\rho_i H_\phi^{n+1/2}(i, j) \end{array} \right] \qquad (3.6)$$

$$H_\phi^{n+1/2}(i, j) = H_\phi^{n-1/2}(i, j) + \frac{\Delta t}{\mu_0} \left[\begin{array}{c} \dfrac{E_z^n(i+1/2, j) - E_z^n(i-1/2, j)}{\Delta \rho} \\ -\dfrac{E_\rho^n(i, j+1/2) - E_\rho^n(i, j-1/2)}{\Delta z} \end{array} \right] \qquad (3.7)$$

Since the modes excited for the catheter's coaxial feedline are TEM modes which, in cylindrical coordinates, include only the E_ρ and H_ϕ components only the rotationally symmetric TM modes are excited which include the components E_ρ, E_z and H_ϕ.

3.4.   Proposed Design and Results

While MW ablation shows promise, there exists several shortcomings that ought to be overcome for this method of ablation to undergo practical implementation. The first of which is adequate impedance match. To illustrate the effects impedance matching can have on the performance of the catheter, its coaxial cable is initially modeled as a transmission line in (3.8 - 3.9).

$$V(z) = V_0 e^{-\gamma z}(1 + \Gamma e^{2\gamma z}) \tag{3.8}$$

$$I(z) = V_0 e^{-\gamma z}(1 - \Gamma e^{2\gamma z})/Z_0 \tag{3.9}$$

Where the time average power density is expressed as (3.10) and the power dissipated (P_d) per unit length is given by (3.11):

$$P = V_0^2 e^{-2az}(1 - |\Gamma| e^{4az})\text{Re}(1/2Z_0) \tag{3.10}$$

$$P_d = -\partial P / \partial z \tag{3.11}$$

At a perfect impedance match the reflection coefficient $\Gamma = 0$ and the power dissipated per unit length is reduced to (3.12) clearly illustrating the extent of impedance match dependence.

$$P_d = 2\alpha P \tag{3.12}$$

In order to provide a measure of the extent of impedance match, frequency domain analysis becomes necessary. This entails the use of the following Fourier transform equation for the electric field at a given frequency f_k as a first step towards obtaining the reflection coefficient.

26

$$e(f_k) = \int\limits_{-\infty}^{\infty} E(t)e^{-j2\pi f_k t}dt \qquad (3.13)$$

where discretizing (3.13) would give rise to the Discrete Fourier Transform (DFT) given
by (3.14).

$$e(f_k) = \Delta t \sum_{n=0}^{N-1} E(n\Delta t)e^{-j2\pi f_k \Delta t} \qquad (3.14)$$

Lastly, the reflection coefficient and the corresponding return loss (RL) is given by
(3.15 - 3.16).

$$\Gamma(f) = \frac{\left| DFT(E_{i,j,k}^{total} - E_{i,j,k}^{inc}) \right|}{\left| DFT(E_{i,j,k}^{inc}) \right|} \qquad (3.15)$$

$$RL = 20\log_{10}\left|\Gamma\right| \qquad (3.16)$$

A three-dimensional rendition of the catheter and a cross sectional view are depicted in
Figs. 6(a) and 6(b) respectively.
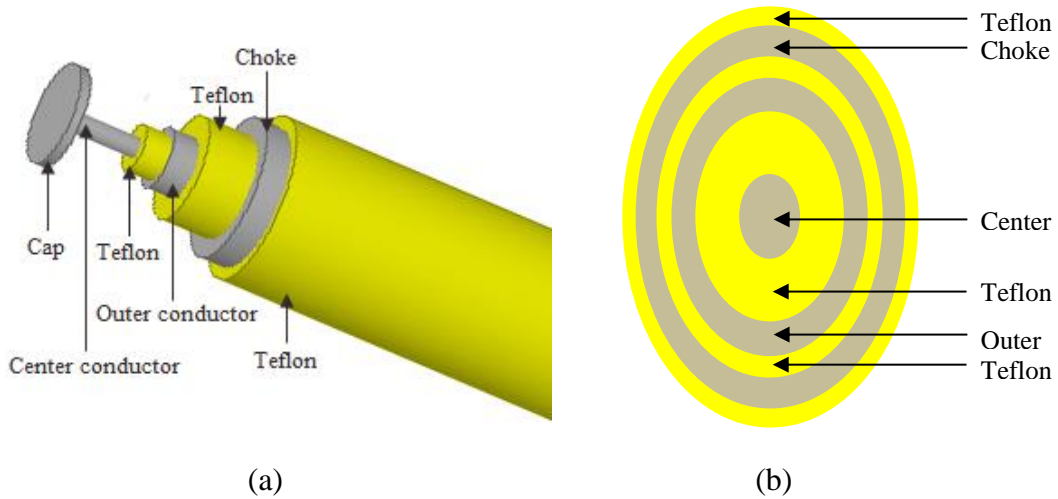

(a)   (b)

Fig. 6. Renditions of microwave catheter (a) Three-dimensional (b) Cross sectional

The design departs from a microwave monopole where the resonant frequency is that at which the return loss is minimum. Its outline and dimensions are depicted in Fig. 7 where it is useful to remind the reader that due to the rotational symmetric nature of the structure, only half of it will be simulated whilst still providing valid solutions for the entire structure.
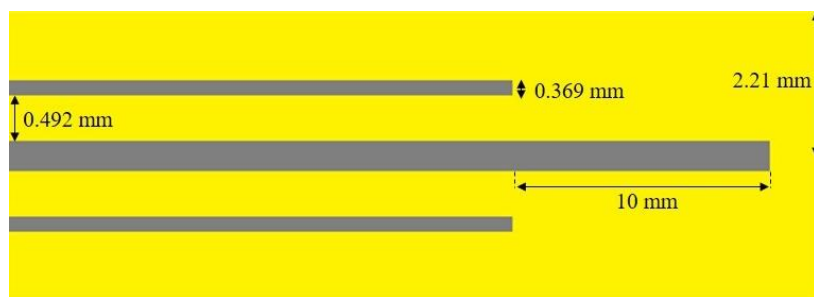

Fig. 7. Dielectric coated monopole

Throughout all simulations in this thesis, the catheter will be immersed in a background material mimicking blood. The simple dielectric coated monopole's return loss bandwidth along with its SAR distribution are depicted in Figs. 8 and 9 respectively.
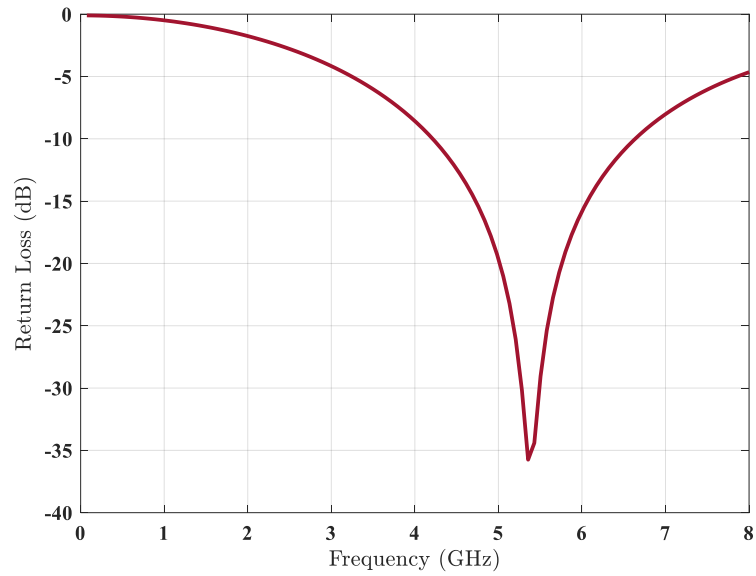
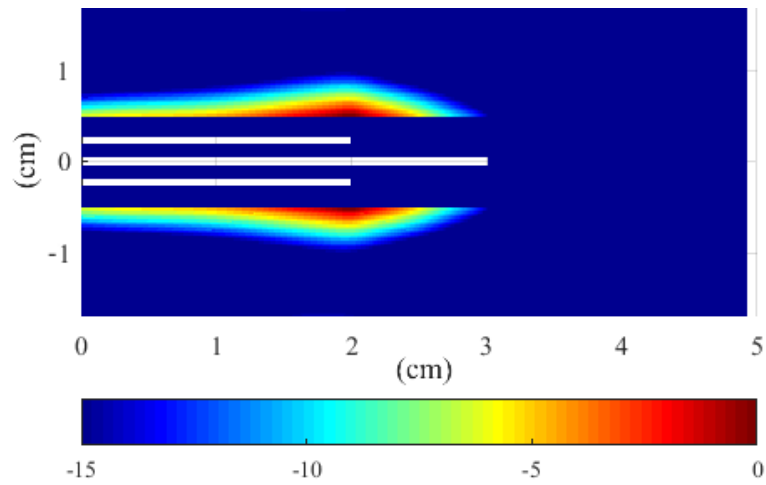Fig. 8. Dielectric coated monopole return loss bandwidth

Fig. 9. Dielectric coated monopole SAR distribution

Ultimately, the goal is to design a compact catheter operating at a frequency that is at, or as close as possible to, 2.45 GHz as this is the frequency at which most power is absorbed within the tissue of interest. Clearly, from Figs. 8 and 9 two problems are

evident with the simple dielectric coated monopole, otherwise known as sleeved

monopole case. The first of which is that the operating frequency is almost double of the

frequency of interest. Furthermore, while it is shown in [9] that the Teflon coating

prevents radiation hot spots from taking place at the junction between the antenna and

feed line, nonetheless some power couples into a leaky wave thereby travelling at the

periphery of the catheter and within the sheath. This is an issue of grave importance as it

may produce unwanted backwards heating resulting in unwelcome ablation of healthy

tissue. To address the issue of operating frequency, a terminating disk is added to the

end of the monopole. Its dimensions, return loss bandwidth and normalized SAR pattern

are depicted in Figs. 10, 11 and 12 respectively.

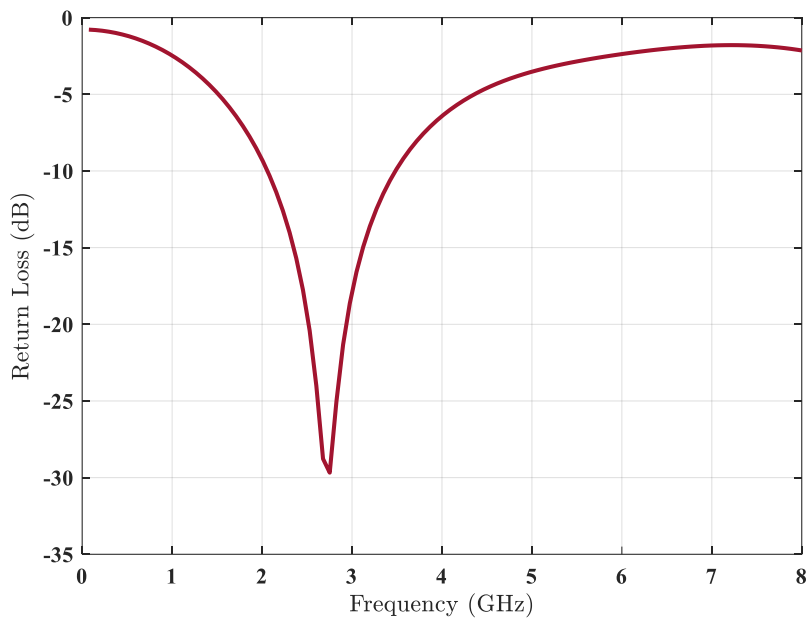Fig. 10. Dielectric coated monopole with terminating cap

Fig. 11. Dielectric coated monopole with terminating cap return loss bandwidth
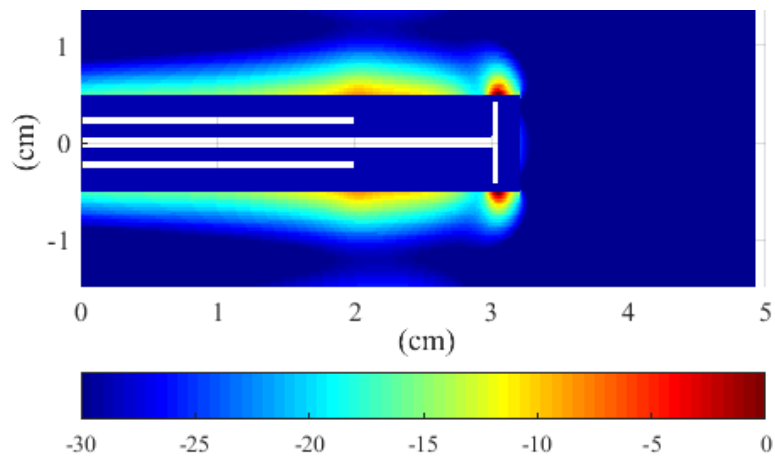

Fig. 12. Dielectric coated monopole with terminating cap SAR distribution

This in essence, is a form of dipole loading which allows ESAs to appear electrically larger whilst achieving the desired effect of reducing, almost halving, the

31

center frequency. A return loss comparison of the monopole with and without the
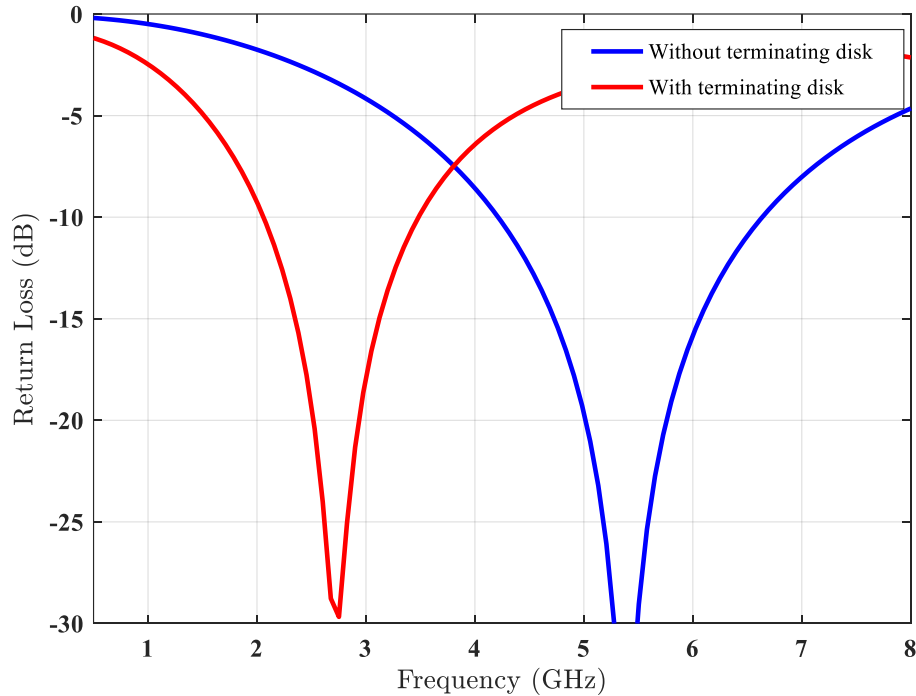
terminating disk is depicted in Fig. 13.

Fig. 13. Comparison of return loss bandwidth for catheter with/without terminating cap

While the issue of frequency of operation is addressed using the end cap, the

issue of eliminating power coupling into leaky waves on the periphery and within the

catheter's Teflon sheath remains. It is necessary to emphasize the extent to which this

particular issue is important. For this reason, a sleeve choke is introduced to address this

issue. In addition, two structures introduced in literature aimed at addressing this issue

are also examined. A lateral cross section of the catheter with a terminating cap and a
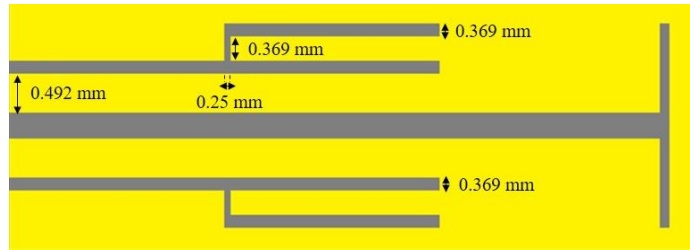
sleeve choke is shown in Fig. 14.

Fig. 14. Monopole with terminating cap and sleeve choke

This addition proves to be highly effective with near complete elimination of leaky waves. Its return loss bandwidth and SAR distribution are both depicted in Fig. 15 and 16 respectively.
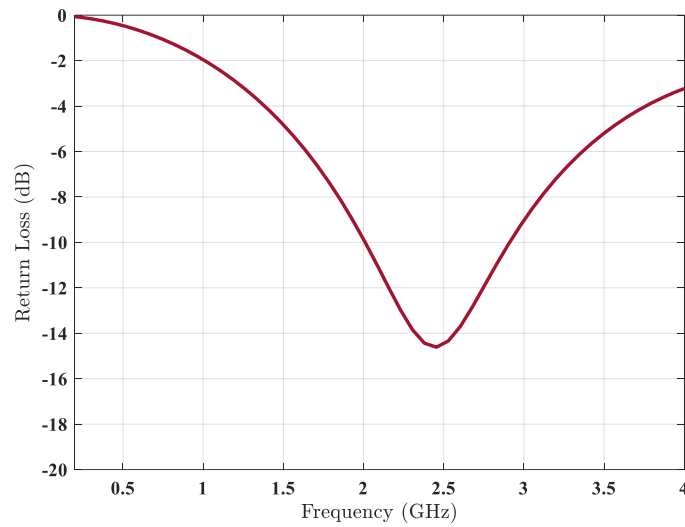

Fig. 15. Monopole with terminating cap and sleeve choke return loss bandwidth
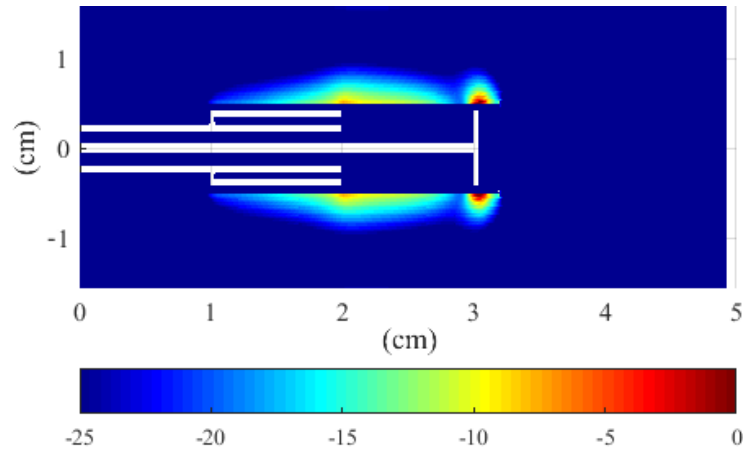
Fig. 16. Monopole with terminating cap and sleeve choke SAR distribution

It is however worth noting that there appears to be a significant impact on return loss where despite meeting the conditions of a VSWR that is less than two, the extent of reflection contracts from a negligible 0.1 % reflection to a more significant 3.16 % but acceptable nonetheless. Typically, acceptable reflection is 10 % or less. Other undertakings related to MW ablation as in [10] claim a more superior sleeve-choke mechanism. The proposed mechanism entails removing the physical connection between the sleeve choke and outer conductor thereby giving rise to the floating sleeve. Further investigation into the authors' proposed floating sleeve structure have indeed yielded a much more superior return loss as is depicted in Fig. 17.
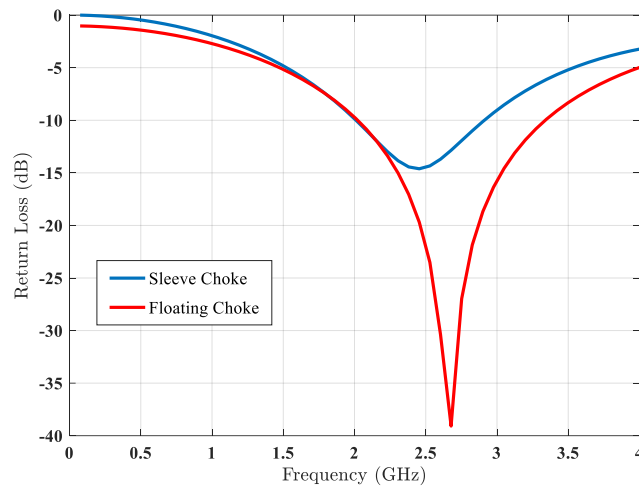
Fig. 17. Comparison of return loss bandwidth for sleeve choke and floating choke

However, SAR analysis has revealed the existence of power coupling into leaky waves on the periphery and within the Teflon sheath. This is depicted in Fig. 18.
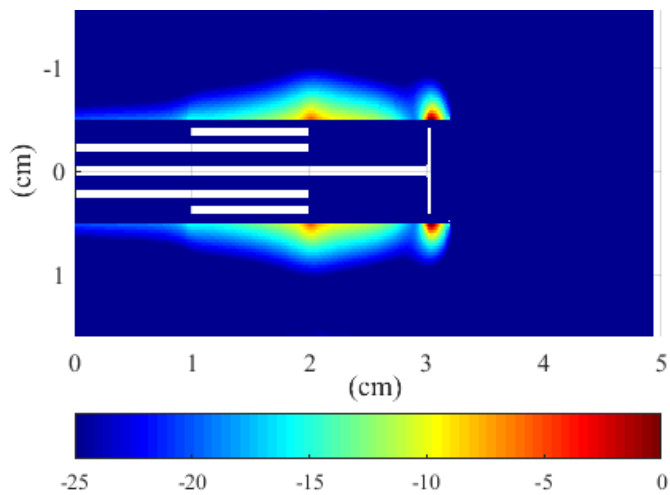
Fig. 18. Floating sleeve SAR distribution

Furthermore, FDTD radiated power analysis has also revealed that the power within the exterior Teflon sheath of the catheter employing the floating sleeve is consistently larger than that of the catheter employing a sleeve choke. The results of this analysis are depicted in Fig. 19.

(a)

$$\left(\frac{P_{FloatingChoke} - P_{SleeveChoke}}{P_{SleeveChoke}}\right) \times 100\%$$

(b)
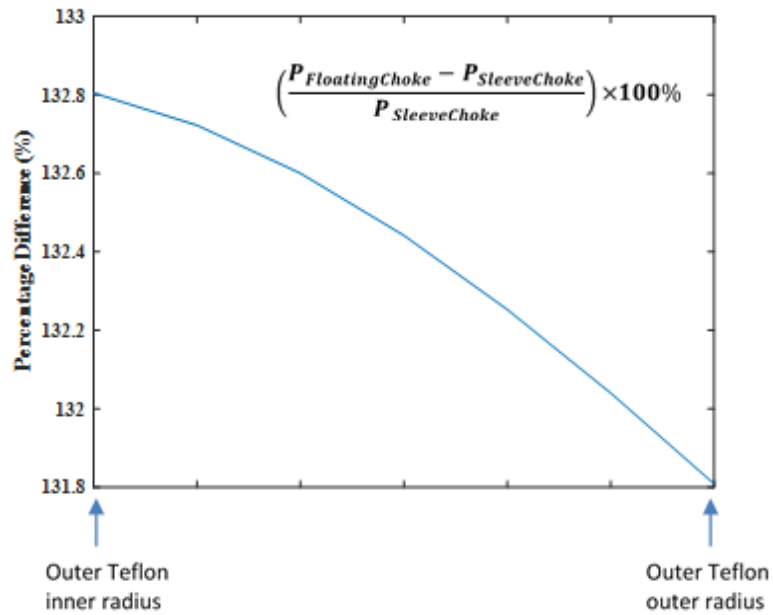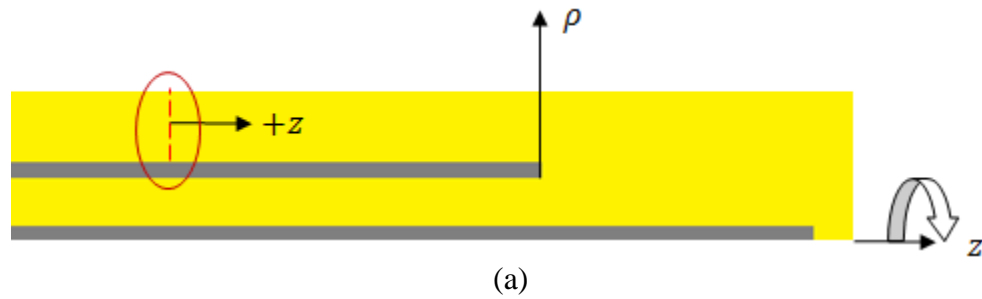
Fig. 19. Power within outer Teflon layer comparison

From Fig. 19 it is evident that at varying radial distances beginning at the outer Teflon sheath's inner radius and ending at the outer Teflon sheath's outer radius power is consistently larger with the floating sleeve case compared to the sleeve choke case. This too is a source for concern, as excess power within the Teflon sheath can result in excess heating of that layer along with tissue adjacent to it.

The second structure proposed in literature that was adapted to the existing structure was the internally matched catheter proposed in [11]. Its return loss bandwidth along with the relevant SAR distribution are both depicted in Figs. 20 and 21 respectively.

Fig. 20. Bandwidth comparison between sleeve choke and internal match
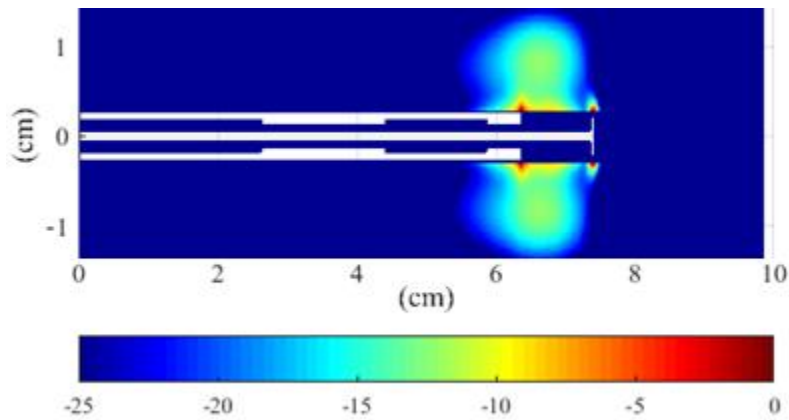
Fig. 21. Internally matched catheter SAR distribution

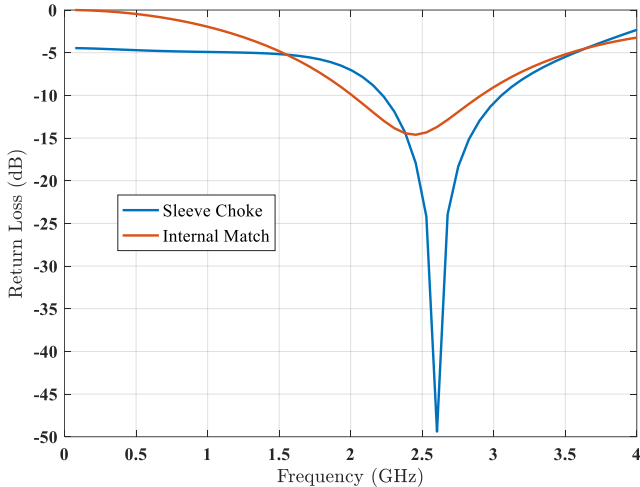The internal matching mechanism substitutes the exterior chokes all together. This internal matching mechanism can in fact be modeled as a pi network comprising of two parallel capacitors separated by a series inductor. This particular design capitalizes on the creation of a high impedance point that acts as natural choke point thereby prohibiting power from coupling into leaky waves and flowing on the surface of the coaxial line. The high impedance point from the input side can be matched to the impedance of the coaxial line feeding the microwave probe through proper design of the pi network. Indeed, looking at that SAR distribution depicted in Fig. 21 this mechanism appears to be highly effective at eliminating surface waves while also attaining high impedance match between the coaxial line and the microwave probe. It also has the added advantages of improving the extent and general distribution of power deposited within the adjacent tissue.

As a final undertaking aimed towards optimizing the catheter's performance, a dielectric plug is introduced to the structure as shown in Fig. 22.
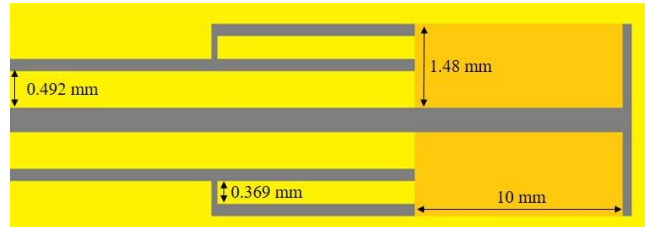
Fig. 22. Monopole with terminating cap, sleeve choke and dielectric plug

It is chosen to have a higher dielectric constant, $\varepsilon_r = 12$, than that of Teflon and is aimed at electrically shortening wavelength which in turn would lower the operating frequency. The return loss bandwidth and SAR distribution are both depicted in Figs. 23 and 24 respectively.
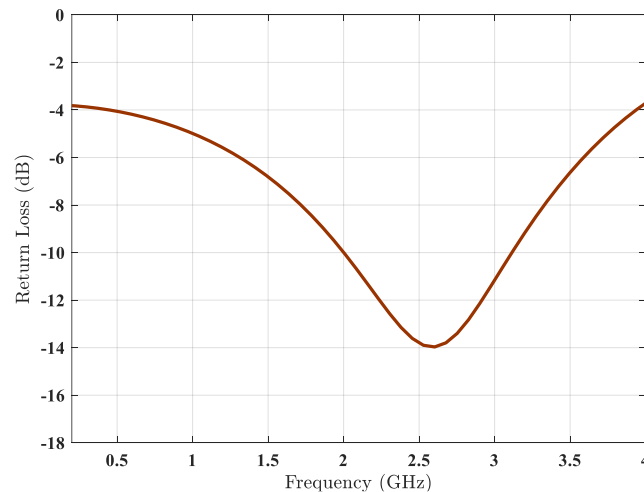
Fig. 23. Monopole with terminating cap, choke and dielectric plug return loss bandwidth
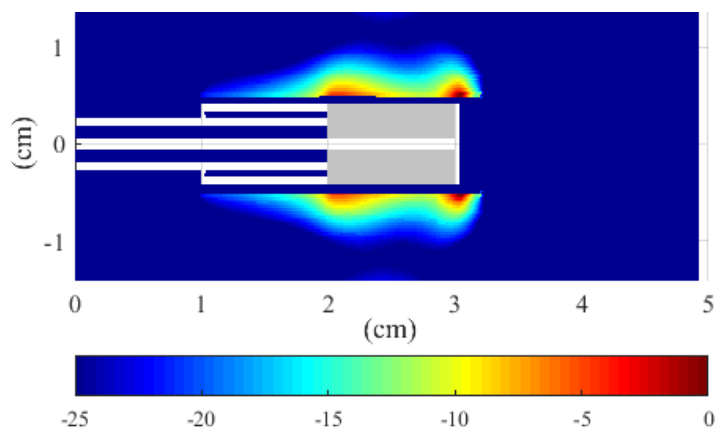
Fig. 24. Monopole with cap, choke and dielectric plug SAR distribution

A further study aimed at observing the effects of dielectric constant variations within the plug are also presented in Fig. 25.
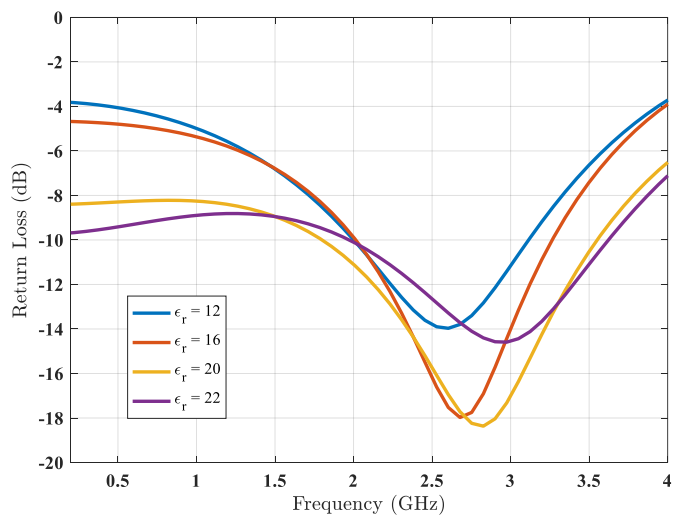
Fig. 25. Return loss bandwidth for varying dielectric permittivities

The results indicate that the plug had limited effectiveness in resulting in any significant variations in the catheter's return loss. However, from Fig. 24 lateral improvements in the SAR distribution are observable. Another noticeable advantage is an increase in bandwidth. This is of particular importance as the dielectric properties of blood undergo slight variations from one individual to another, therefore it may not be a universal truth that the frequency at which most radiation absorption take place is 2.45 GHz. For this reason, increases in bandwidth facilitated by the dielectric plug allow for that margin of variation without compromising the effectiveness of the catheter as a whole. Parameters pertaining to bandwidth, quality factor and center frequency for the various structures introduced in this section are summarized in Table 2.

Table 2 - Performance metrics for various structures introduced

Structure	f_c (GHz)	min. RL (dB)	B_{VSWR} (%)	Q_{VSWR}
Monopole without disk	5.35	-35.75	47.29	2.11
Monopole with disk	2.75	-29.68	54.40	1.84
Monopole with disk and sleeve choke	2.45	-14.61	36.73	2.72
Monopole with disk - floating choke	2.68	-39.08	50.26	1.99
Monopole with disk - internal match	2.60	-49.39	34.35	2.91
Monopole with disk, choke and plug	2.6	-13.97	43.08	2.32

3.5.   *Near to Far Field Transformation*

As mentioned earlier, due to practical constraints the numerical space in which all FDTD simulations take place is finite in extent. However, in practice one would often be interested in far field behavior of structure of interest. Near to far field transformations allow for such analysis. Through this formulation, we can solve for either the scattered field of an obstacle, or for the radiation pattern of the structure from which the radiation has originated; the latter will be of interest in this section. All subsequent formulation will depart from the equivalence principle. This principle attempts to exploit the fact that several sources outside a given closed region can give rise to the same fields within that region. Two sources of radiation which give rise to the same set of fields within a region are called equivalent [12]. Consider the following set of boundary conditions:

$$\hat{n} \times \overrightarrow{H} = \overrightarrow{J}_{eq} \tag{3.17}$$

$$\overrightarrow{E} \times \hat{n} = \overrightarrow{M}_{eq} \tag{3.18}$$

In a region where a source radiates a set of fields we can define a fictitious boundary that surrounds that source. Next, the fields within this boundary are set to zero and are replaced by a set of currents on the boundary. Finally, the fictitious currents are used to find the fields outside the boundary surrounding the object which had been removed.

Consider the case in which an object exists in the numerical space as depicted in Fig. 26.
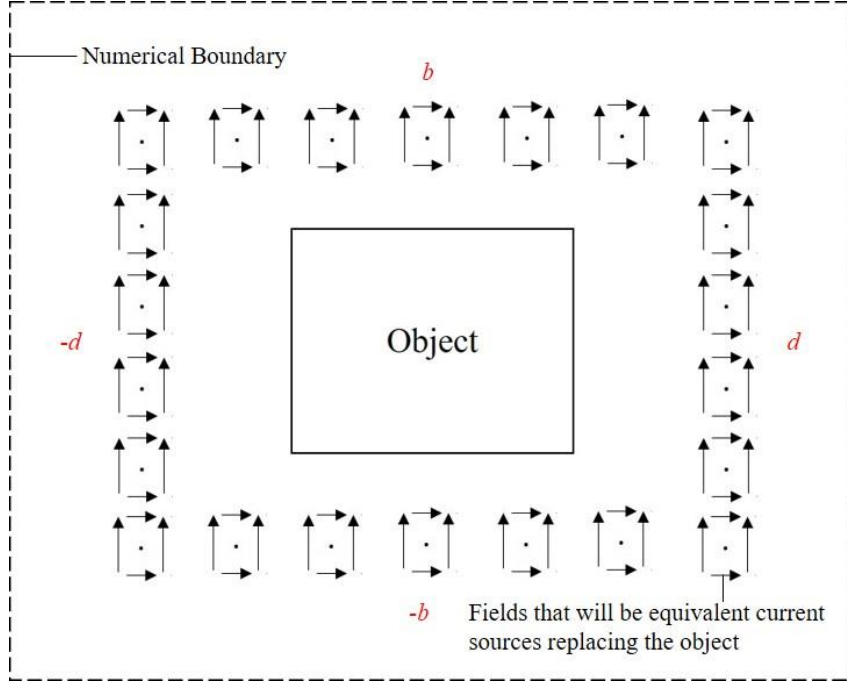
Fig. 26. Equivalence principle

The following formulation would ultimately lead to an expression for the far field electric field:

At the boundary $\pm b$:

$$\left(\hat{z}\times\left[\pm y\times\breve{E}_z\hat{z}\right]\right)\cdot\left(\cos\phi x+\sin\phi y\right)=\pm\breve{E}_z\sin\phi \tag{3.19}$$

$$\pm y\times\left(\breve{H}_x x+\breve{H}_y y\right)=\mp\breve{H}_x\hat{z} \tag{3.20}$$

At the boundary $\pm d$:

$$\left(\hat{z} \times \left[\pm x \times \breve{E}_z \hat{z}\right]\right) \cdot \left(\cos\phi x + \sin\phi y\right) = \pm \breve{E}_z \cos\phi \qquad (3.21)$$

$$\pm x \times \left(\breve{H}_x x + \breve{H}_y y\right) = \pm \breve{H}_y \hat{z} \qquad (3.22)$$

In turn this allows for the construction of a boundary around which a magnetic current flows that replaces the fields within the enclosed region. This is depicted in Fig. 27.

Fig. 27. Obstacle replacement using equivalence principle

Finally, the far field is described by the set of line integrals given by (3.23) and are later discretized as (3.24).

$$
\begin{aligned}
\breve{E}_z^{norm}(r) = & \int_{-b}^{b}\left[\eta_0\breve{H}_y(r') - \breve{E}_z(r')\cos\phi\right]\cdot e^{jk(d\cos\phi + y'\sin\phi)}dy' \\
& + \int_{d}^{-d}\left[-\eta_0\breve{H}_x(r') - \breve{E}_z(r')\sin\phi\right]\cdot e^{jk(x'\cos\phi + b\sin\phi)}dx' \\
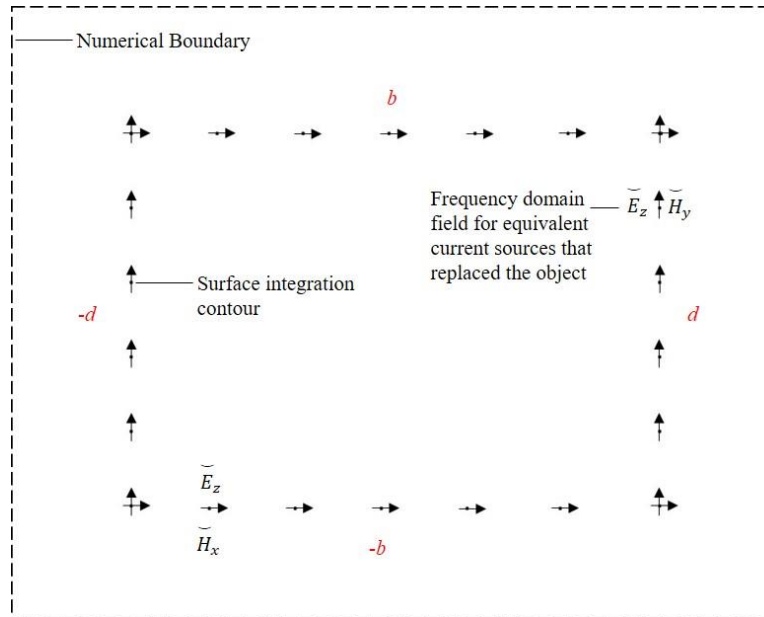& + \int_{b}^{-b}\left[-\eta_0\breve{H}_y(r') - \breve{E}_z(r')\cos\phi\right]\cdot e^{jk(-d\cos\phi + y'\sin\phi)}dy' \\
& + \int_{-d}^{d}\left[\eta_0\breve{H}_x(r') - \breve{E}_z(r')\sin\phi\right]\cdot e^{jk(x'\cos\phi - b\sin\phi)}dx'
\end{aligned}
\tag{3.23}
$$

$$
\begin{aligned}
\breve{E}_z^{norm}(r) = & \sum_{j=js}^{jn}\left[\eta_0\breve{H}_{yin,j} - \breve{E}_{zin,j}\cos\phi\right]\cdot e^{jk(d\cos\phi + y_j\sin\phi)}\Delta_j \\
& + \sum_{i=is}^{in}\left[-\eta_0\breve{H}_{xi,jn} - \breve{E}_{zi,jn}\sin\phi\right]\cdot e^{jk(x_i\cos\phi + b\sin\phi)}\Delta_i \\
& + \sum_{j=js}^{jn}\left[-\eta_0\breve{H}_{yis,j} - \breve{E}_{zis,j}\cos\phi\right]\cdot e^{jk(-d\cos\phi + y_j\sin\phi)}\Delta_j \\
& + \sum_{i=is}^{in}\left[\eta_0\breve{H}_{xi,js} - \breve{E}_{zi,js}\sin\phi\right]\cdot e^{jk(x_i\cos\phi - b\sin\phi)}\Delta_i
\end{aligned}
\tag{3.24}
$$

A similar boundary problem can be constructed around the catheter as shown in Fig. 28.
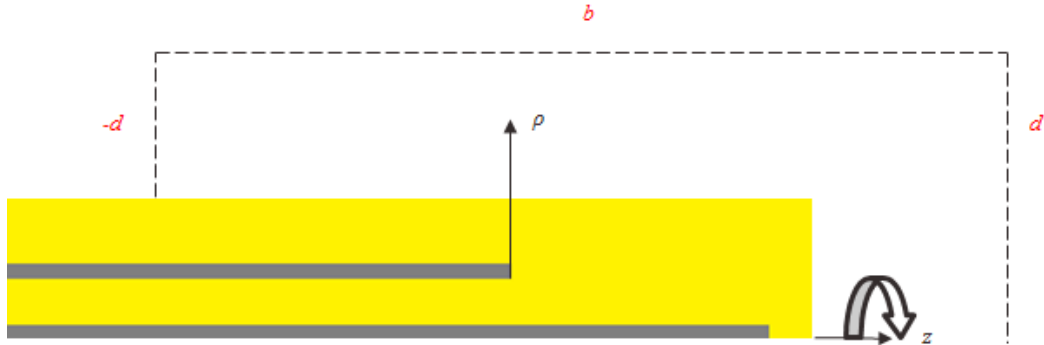
Fig. 28. Boundary around catheter for near to far field transformation

A near-to-far-field transformation analysis similar to that conducted on the object can be conducted on the catheter in cylindrical co-ordinates and would result in the following equation through which the catheter's radiation pattern can be obtained.

$$
\begin{aligned}
\breve{H}_\phi^{norm}(\theta) &= \sum_{i=is}^{in}\left[-\frac{1}{\eta}\breve{E}_z(b,z') - \breve{H}_\phi(b,z')\sin\theta\right]\cdot J_0\left(kb\sin\theta\right)\cdot e^{jkz'\cos\theta}\Delta \\
&+ \sum_{j=1}^{jn}\left[\frac{1}{\eta}\breve{E}_\rho(\rho',s) + \breve{H}_\phi(\rho',\mathrm{d})\cos\theta\right]\cdot J_0\left(k\rho'\sin\theta\right)\cdot e^{jkd\cos\theta}\Delta \\
&+ \sum_{j=1}^{jn}\left[-\frac{1}{\eta}\breve{E}_\rho(\rho',-\mathrm{d}) - \breve{H}_\phi(\rho',-\mathrm{d})\cos\theta\right]\cdot J_0\left(k\rho'\sin\theta\right)\cdot e^{-jkd\cos\theta}\Delta
\end{aligned}
\tag{3.25}
$$

The normalized radiation pattern in polar co-ordinates and on a Cartesian scale is shown in Figs. 29(a - b) and 30 respectively.

(a)
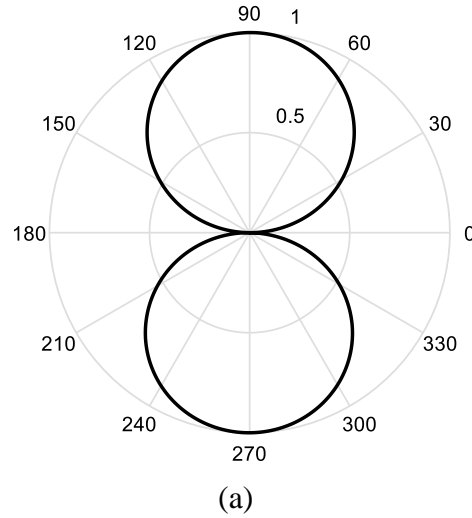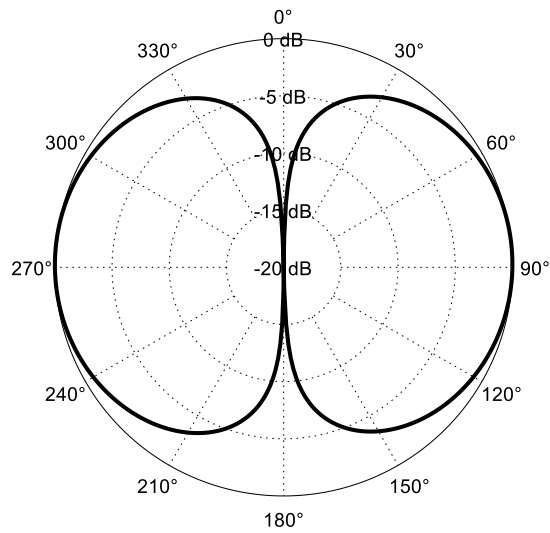
(b)

Fig. 29. Catheter radiation pattern on a polar plot

Angle in Degrees
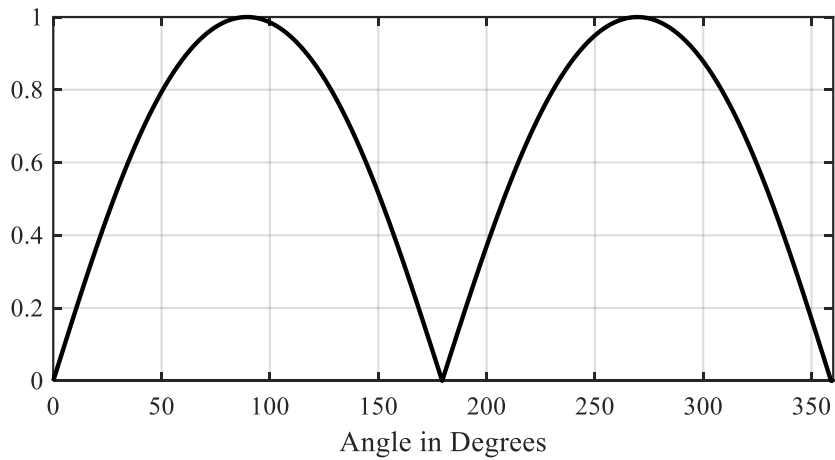
Fig. 30. Catheter radiation pattern in Cartesian co-ordinates

The usefulness of such analysis can be attributed to confirming results associated with

power analysis and associated with the overall function as well as operation of the

catheter.

CHAPTER IV

FDTD MODELLING OF METAMATERIALS

In its most loosely defined sense, a metamaterial is a structure that exhibits characteristics, predominantly electromagnetic, that do not exist in nature and at many instances are highly counter intuitive. They can comprise of novel materials, or composite structures whose interaction gives rise to these characteristics. Such structures are typically periodic, and their characteristics depend on overall size, shape, orientation as well as geometry. The following chapter will attempt to provide an overview of metamaterials in general, outline its modelling using FDTD and attempt to investigate its application in the context of MW catheters in the form of a metamaterial plug.

4.1.   *Fundamentals of Metamaterials*

A large class of metamaterials is often referred to as left handed materials (LHM) owing to the fact that the field vectors would follow a left-handed system, a terminology that was first introduced by Veselago in his 1968 paper [13]. In this paper he puts forth the question as to what consequences would be associated with a material with novel characteristics. The consequences include a refraction index which is negative, evanescent waves would increase in intensity as they get farther away from the source and electric and magnetic fields that would form a left-handed triplet with respect to the direction of phase propagation rather than a traditional right handed triplet [14].

With regards to the index of refraction Veselago concludes that for a traditional medium with an index of refraction $n > 0$ the angle of refraction would have the same sign as the angle of incidence whereas for a medium with an index of refraction $n < 0$ the angle of refraction would have a negative polarity. Furthermore, as a wave propagates through a traditional medium phase delay as a function of the dielectric properties of the medium is expected to be experienced by the wave. In contrast, wave propagation through a metamaterial would yield phase advancement. Based on this idea Pendry in [15] suggests that as propagating waves change into evanescent waves they would undergo growth rather than attention. Here it is appropriate to emphasize that the observation of these physical phenomena is limited by the realization of materials with such characteristics in practice.

4.2.   *Dispersive FDTD*

It is common practice to assume that the dielectric properties of a given material are constant. However, this is rarely the case and is often a function of several factors including but not limited to, frequency. In fact, a dielectric that is both lossless and has constant dielectric properties does not exist in nature. It can be shown that a material with dielectric properties that deviate from those of free space, the imaginary part typically suggesting loss as a function of frequency, cannot be zero for all frequencies. In the interest of satisfying causality the loss may be arbitrarily small. In a situation where permittivity and/or permeability of a given material vary as a function of frequency the material is said to be dispersive. Drude models are widely accepted as one

of the most versatile means of describing such frequency dependent behavior [16]. In this model charges are assumed to move under the influence of an electric field whilst experiencing a damping force as well.

Physicists often use mechanical spring models to describe such behavior. However, for our purposes the Drude model suffices and assumes the following form:

$$\varepsilon(\omega) = \left[1 - \frac{\omega_{pe}^2}{\omega(\omega - j\nu_e)}\right] \tag{4.1}$$

$$\mu(\omega) = \left[1 - \frac{\omega_{pm}^2}{\omega(\omega - j\nu_m)}\right] \tag{4.2}$$

ω_{pe} : Electronic plasma frequency

ω_{pm} : Magnetic plasma frequency

ν_e : Electric collision frequency

ν_m : Magnetic collision frequency

For a lossless metamaterial ν_e is equal to ν_m and are both equal to zero. However, losses can easily be accounted for once the main dispersive FDTD code has been formulated, through the electric collision and magnetic collision frequency. For the purposes of demonstration consider the standard Drude profile for Drude permittivity for various extents of losses depicted in Fig. 31.
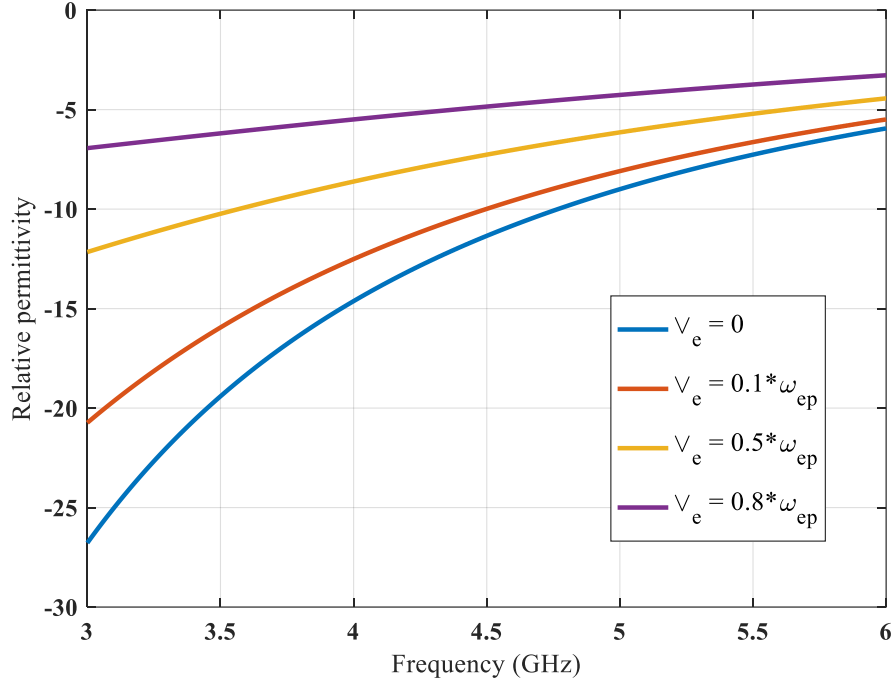
Fig. 31. Drude permittivity profile for various extents of loss

A lossless case corresponds to electric collision and magnetic collision frequency being set to zero and this will be case of interest [17]. The next step would be to account for the dispersive nature of metamaterials through writing Maxwell's equations accordingly followed by discretizing those equations for FDTD implementation using the second order central difference theorem. We will only be concerned with the two-dimensional TM case.

$$\frac{\partial D_z}{\partial t} = \frac{\partial H_y}{\partial x} - \frac{\partial H_x}{\partial y} \qquad (4.3)$$

$$D_z = \varepsilon_0 \left[1 - \frac{\omega_{pe}^2}{\omega(\omega - j\nu_e)} \right] E_z \qquad (4.4)$$

51

$$\frac{\partial B_x}{\partial t} = -\frac{\partial E_z}{\partial y} \tag{4.5}$$

$$B_x = \mu_0 \left[1 - \frac{\omega_{pm}^2}{\omega(\omega - j\nu_m)} \right] H_x \tag{4.6}$$

$$\frac{\partial B_y}{\partial t} = \frac{\partial E_z}{\partial x} \tag{4.7}$$

$$B_y = \mu_0 \left[1 - \frac{\omega_{pm}^2}{\omega(\omega - j\nu_m)} \right] H_y \tag{4.8}$$

Note, that the multiplication of $j\omega$ terms within the frequency domain entails a

differentiation in the time domain yielding the set of equations shown below.

$$\frac{\partial^2 D_z}{\partial t^2} + \nu_e \frac{\partial D_z}{\partial t} = \varepsilon_0 \frac{\partial^2 E_z}{\partial t^2} + \varepsilon_0 \nu_e \frac{\partial E_z}{\partial t} + \varepsilon_0 \omega_{pe}^2 E_z \tag{4.9}$$

$$\frac{\partial^2 B_x}{\partial t^2} + \nu_m \frac{\partial B_x}{\partial t} = \mu_0 \frac{\partial^2 H_x}{\partial t^2} + \mu_0 \nu_m \frac{\partial H_x}{\partial t} + \mu_0 \omega_{pm}^2 H_x \tag{4.10}$$

$$\frac{\partial^2 B_y}{\partial t^2} + \nu_m \frac{\partial B_y}{\partial t} = \mu_0 \frac{\partial^2 H_y}{\partial t^2} + \mu_0 \nu_m \frac{\partial H_y}{\partial t} + \mu_0 \omega_{pm}^2 H_y \tag{4.11}$$

Now, the final step is to discretize the equations (4.5 - 4.8) and (4.9 - 4.11) for FDTD

implementation.

$$D_z^{n+1}(i+1/2, j+1/2) = D_z^n(i+1/2, j+1/2) + \frac{\Delta t}{\Delta x} [H_y^{n+1/2}(i+1, j+1/2)$$
$$-H_y^{n+1/2}(i, j+1/2)] - \frac{\Delta t}{\Delta y} [H_x^{n+1/2}(i+1/2, j+1) - H_x^{n+1/2}(i+1/2, j)] \tag{4.12}$$

$$E_z^{n+1}(i{+}1/2, j{+}1/2) = \frac{1}{\varepsilon_0(2+\nu_e\Delta t)}[(2+\nu_e\Delta t)\,\mathrm{D}_z^{n+1}(i+1/2, j+1/2)$$

$$-4\,\mathrm{D}_z^n(i+1/2, j+1/2)+(2-\nu_e\Delta t)\,\mathrm{D}_z^{n-1}(i+1/2, j{+}1/2)- \qquad (4.13)$$

$$2\varepsilon_0(\omega_{pe}^2\Delta t^2 - 2)E_z^n(i+1/2, j{+}1/2)-\varepsilon_0(2-\nu_e\Delta t)E_z^{n-1}(i+1/2, j{+}1/2)$$

$$B_x^{n+3/2}(i+1/2, j) = B_x^{n+1/2}(i+1/2, j)-(\Delta t / \Delta y)[E_z^{n+1}(i{+}1, j{+}1/2)$$

$$-E_z^{n+1}(i{+}1/2, j{-}1/2)] \qquad (4.14)$$

$$H_x^{n+3/2}(i{+}1/2, j) = \frac{1}{\mu_0(2+\nu_m\Delta t)}[(2+\nu_m\Delta t)B_x^{n+3/2}(i+1/2, j)$$

$$-4B_x^{n+1/2}(i+1/2, j)+(2-\nu_m\Delta t)B_x^{n-1/2}(i+1/2, j)- \qquad (4.15)$$

$$2\mu_0(\omega_{pm}^2\Delta t^2 - 2)H_x^{n+1/2}(i+1/2, j)-\mu_0(2-\nu_m\Delta t)H_x^{n-1/2}(i+1/2, j)$$

$$B_y^{n+3/2}(i, j+1/2) = B_y^{n+1/2}(i, j+1/2)-(\Delta t / \Delta x)[E_z^{n+1}(i{+}1/2, j{+}1/2)$$

$$-E_z^{n+1}(i{-}1/2, j+1/2)] \qquad (4.16)$$

$$H_y^{n+3/2}(i, j+1/2) = \frac{1}{\mu_0(2+\nu_m\Delta t)}[(2+\nu_m\Delta t)B_y^{n+3/2}(i, j+1/2)$$

$$-4B_y^{n+1/2}(i, j+1/2)+(2-\nu_m\Delta t)B_y^{n-1/2}(i, j+1/2)- \qquad (4.17)$$

$$2\mu_0(\omega_{pm}^2\Delta t^2 - 2)H_y^{n+1/2}(i, j+1/2)-\mu_0(2-\nu_m\Delta t)H_y^{n-1/2}(i, j+1/2)$$

The proper operation of the given formulation shown above is confirmed by replicating the findings in [18] in which a sinusoidal excitation is placed adjacent to a metamaterial slab. The findings are depicted in Fig. 33.
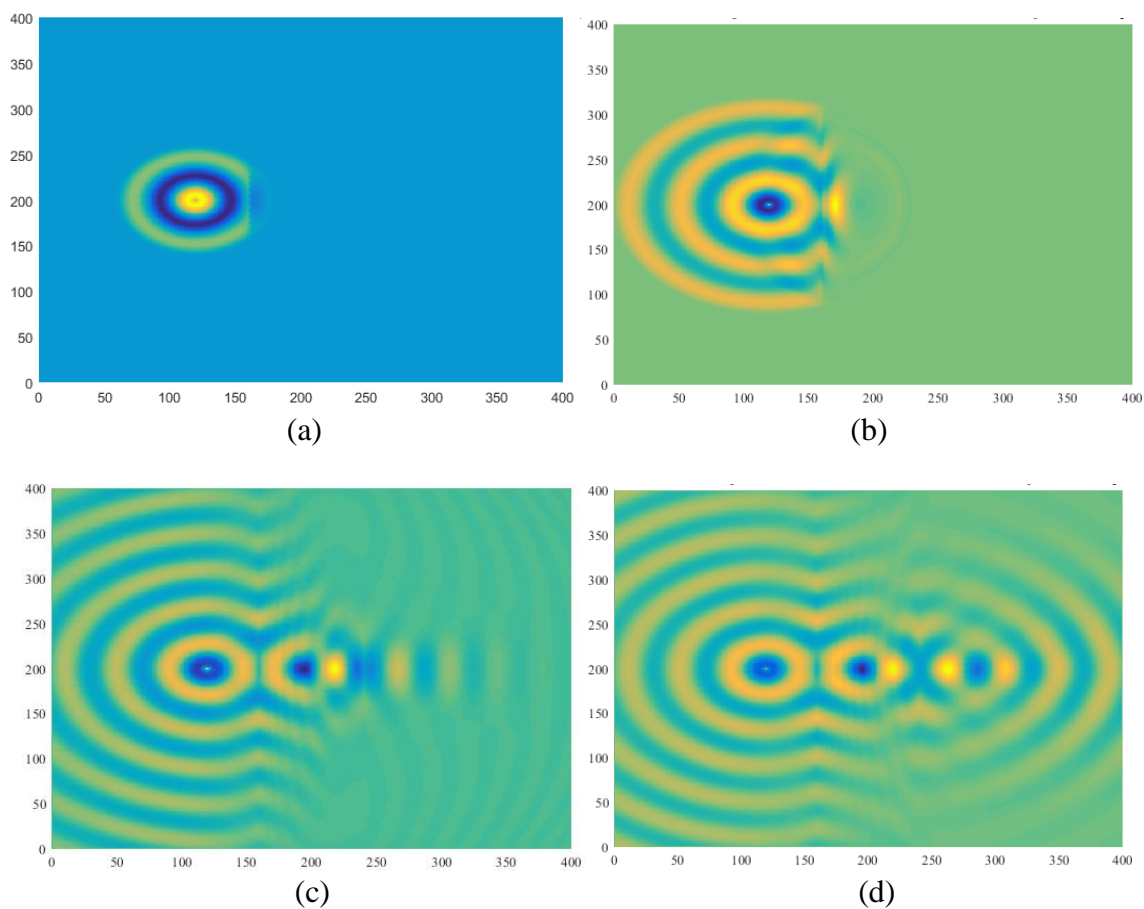
Fig. 32. Sinusoidal excitation adjacent to metamaterial slab at time steps n
(a) n = 90 (b) n = 180 (c) n = 540 (d) 840

It can be noted that the FDTD results illustrate power flow in all directions, otherwise known as monochromatic, through the slab in the form of beams as well as the creation of a focal point. However, Mittra in [19] notes that the creation of this focal point has not been observed for any realistic medium which can be realized in a practical setting.

4.3. Application to Microwave Catheters

In this section, the effect of using metamaterials in the form of a metamaterial plug embedded at the tip of the catheter is investigated. While little improvements were realizable in terms of enhanced return loss, miniaturization possibilities were observed thereby allowing for an overall reduction in the catheter's probe length. The first step aimed at investigating the use of metamaterials in the context of MW catheters was expressing the formulation in Section 4.2 in cylindrical co-ordinates.

To do so, we begin with the following set of equations:

$$\frac{\partial B_\phi}{\partial t} = \frac{\partial E_z}{\partial \rho} - \frac{\partial E_\rho}{\partial z} \tag{4.18}$$

$$B_\phi = \mu_0 \left[1 - \frac{\omega_{pm}^2}{\omega(\omega - jv_m)} \right] H_\phi \tag{4.19}$$

$$\frac{\partial D_z}{\partial t} = \frac{1}{\rho} \frac{\partial (\rho H_\phi)}{\partial \rho} \tag{4.20}$$

$$D_z = \varepsilon_0 \left[1 - \frac{\omega_{pe}^2}{\omega(\omega - jv_e)} \right] E_z \tag{4.21}$$

$$\frac{\partial D_\rho}{\partial t} = -\frac{\partial H_\phi}{\partial z} \tag{4.22}$$

$$D_\rho = \varepsilon_0 \left[1 - \frac{\omega_{pe}^2}{\omega(\omega - jv_e)} \right] E_\rho \tag{4.23}$$

Again, note that the multiplication of $j\omega$ terms with in the frequency domain entails a differentiation in the time domain yielding the set of equations shown below.

$$\frac{\partial^2 B_\phi}{\partial t^2} + v_m \frac{\partial B_\phi}{\partial t} = \mu_0 \frac{\partial^2 H_\phi}{\partial t^2} + \mu_0 v_m \frac{\partial H_\phi}{\partial t} + \mu_0 \omega_{pm}^2 H_\phi \tag{4.24}$$

$$\frac{\partial^2 D_z}{\partial t^2} + v_e \frac{\partial D_z}{\partial t} = \varepsilon_0 \frac{\partial^2 E_z}{\partial t^2} + \varepsilon_0 v_e \frac{\partial E_z}{\partial t} + \varepsilon_0 \omega_{pe}^2 E_z \tag{4.25}$$

$$\frac{\partial^2 D_\rho}{\partial t^2} + v_e \frac{\partial D_\rho}{\partial t} = \varepsilon_0 \frac{\partial^2 E_\rho}{\partial t^2} + \varepsilon_0 v_e \frac{\partial E_\rho}{\partial t} + \varepsilon_0 \omega_{pe}^2 E_\rho \tag{4.26}$$

$$\frac{\partial D_z}{\partial t} = \frac{1}{\rho} \frac{\partial \left(\rho H_\phi \right)}{\partial \rho} \tag{4.27}$$

$$\frac{\partial D_\rho}{\partial t} = -\frac{\partial H_\phi}{\partial z} \tag{4.28}$$

$$\frac{\partial B_\phi}{\partial t} = \frac{\partial E_z}{\partial \rho} - \frac{\partial E_\rho}{\partial z} \tag{4.29}$$

The next step would be to discretize the equations (4.24 - 4.26) and (4.27 - 4.29) for FDTD implementation. This is then followed by a study on the effects of varying negative permittivity and permeability synonymous with left handed materials. The results of the first study are depicted in Fig. 33.
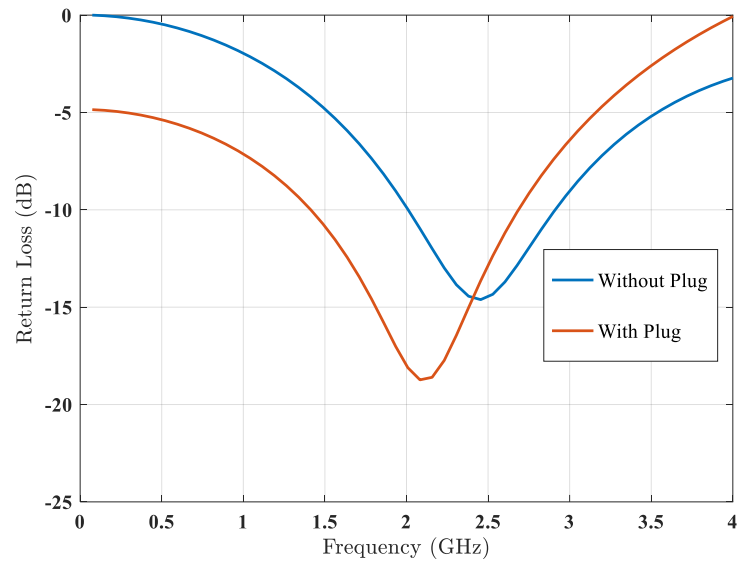
Fig. 33. Return loss bandwidth comparison with/without metamaterial plug

 In terms of return loss improvements, the DNG slab with relative permittivity and permeability equal to -5, the metamaterial plug had limited effects, yielding an improvement of an extra -4 dB at its respective resonant frequency. However, it resulted in a shifting down of the resonant frequency which in turn is synonymous with making the catheter's microwave probe appear electrically longer. This would allow for microwave probe length reductions if for the application of interest this is desirable. In Fig. 33 the microwave probe was fixed to a length of 1 cm. In Fig. 34, the microwave probe's length is reduced to 0.74 cm and the effects of varying the metamaterial plug's permittivity is investigated.
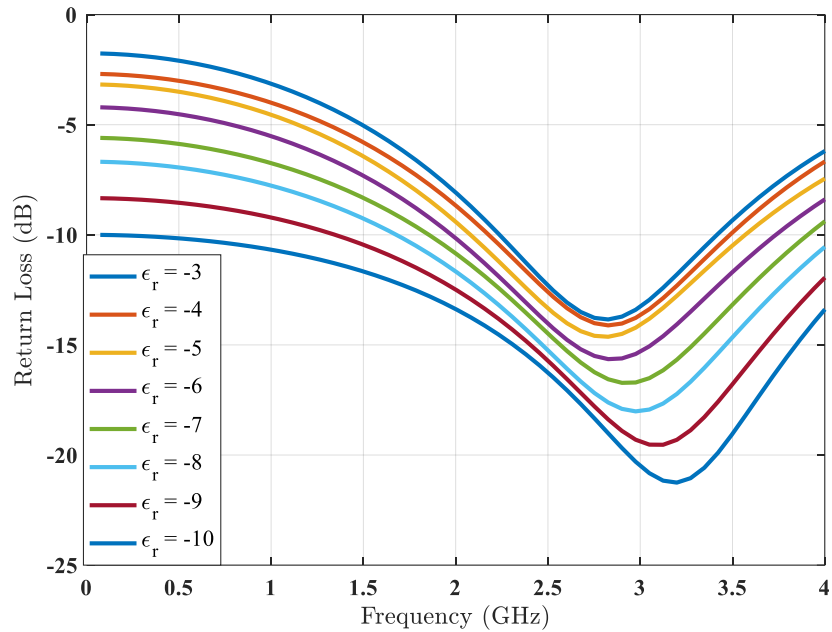
Fig. 34. Return loss bandwidth for varying metamaterial plug permittivities

From Fig. 34 it is evident that increases in permittivity yielded increases in resonant frequency. It can also be noted that such increases were also synonymous with improvements in return loss at resonance. As expected shorter lengths shifted the resonant frequency forward. Length reductions of up to 26% whilst achieving improvements in return loss are shown to be realizable.

It is worth noting that length reduction of up to 51% were realizable with larger permittivity and permeability values,, $\varepsilon_r = \mu_r = -21$ in particular, and the effect of length variations is shown in Fig. 35.
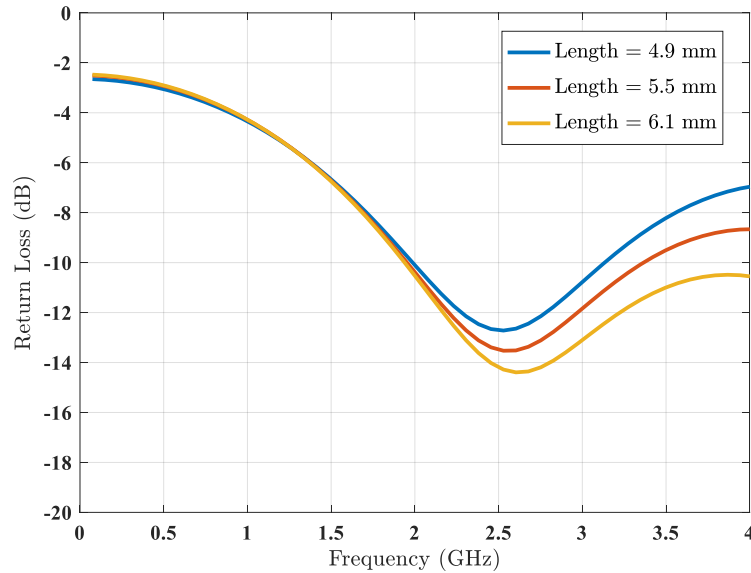
Fig. 35. Effect of length variation on DNG metamaterial plug

In general, no clear effect on return loss is discernable where both improvements and deterioration were noted. Both appeared to be a function of the plug's relative dielectric properties as well as the overall length of the catheter's microwave probe. Furthermore, bandwidth increases were also realizable. This is of particular importance as the dielectric properties of blood undergo slight variations from one individual to another, therefore it may not be a universal truth that the frequency at which most radiation absorption take place is 2.45 GHz. Therefore, increases in bandwidth facilitated by the metamaterial plug allow for that margin of variation without

59

compromising the effectiveness of the catheter as a whole. The structure's SAR

distribution is depicted in Fig. 36.
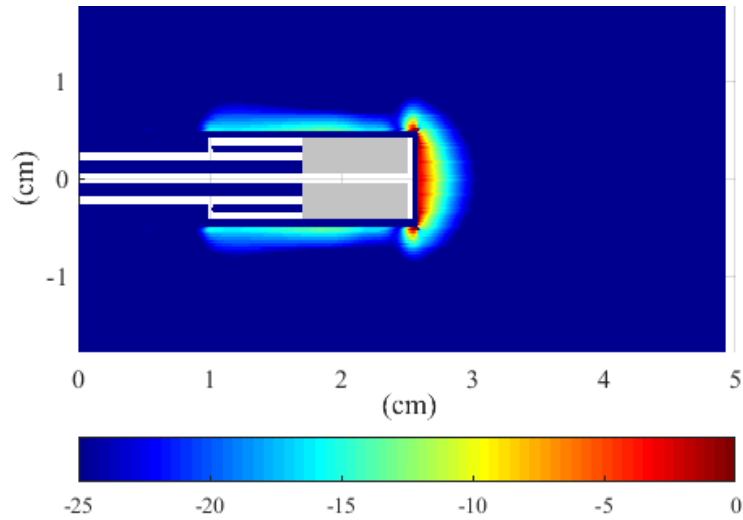
Fig. 36. Catheter with metamaterial plug SAR distribution

Where from Fig. 36 the addition of the metamaterial plug had the effect of

reinforcing and focusing forward radiation towards the catheter's terminating cap. In

applications where the ablation process needs to be highly localized the effect of adding

the metamaterial plug can be desirable; this is inevitably limited by the ability to realize

materials with such properties in practice. Parameters pertaining to bandwidth, quality

factor and center frequency for the various relative permittivities introduced in this

section are summarized in Table 3.

Table 3 - Performance metrics for varying relative permittivities for metamaterial plug

Relative	f_c (GHz)	min. RL (dB)	B_{-3dB} (%)	Q_{VSWR}
$\varepsilon_r = -3$	2.75	-13.77	42.54	2.35
$\varepsilon_r = -5$	2.79	-14.59	53.29	1.88
$\varepsilon_r = -7$	2.91	-16.72	69.31	1.44
$\varepsilon_r = -9$	3.1	-19.53	86.77	1.15
$\varepsilon_r = -18$	2.45	-11.24	47.76	2.09
$\varepsilon_r = -19$	2.53	-13.16	64.82	1.54
$\varepsilon_r = -20$	2.60	-14.39	74.54	1.34
$\varepsilon_r = -21$	2.68	-16.35	80.97	1.24
$\varepsilon_r = -23$	2.90	-20.71	87.66	1.14

From Table 3 it is evident that while a limited range of improvements were realizable in terms return loss, for a fixed microwave probe length increases in relative permittivity yielded a larger fractional bandwidth and a lower quality factor as a consequence.

CHAPTER V

BIOHEAT EQUATION

5.1.   *Fundamentals*

Heat transfer and thermoregulatory responses within the body are highly
complicated processes and are dependent on a wide array of parameters soon to be
discussed. There exists a wide range of models through which such processes can be
modeled. Such models typically fall under two main categories those being active and
passive thermoregulatory control. Classification under the two main categories is
exclusively dependent on whether or not the response to external impulses are taken into
account or not [21]. In general, heat transfer processes within the human body will be
associated with thermal properties, dielectric properties and heat transfer mechanisms
within the tissue.

One of the most versatile means of modeling such processes in the context of
bioheat transfer is one derived by Pennes. This later became known as the bioheat
equation and assumes the following form:

$$\rho C_\rho \frac{\partial T}{\partial t} = \nabla(k\nabla T) - b(T - T_0) + q_m \qquad (5.1)$$

T : Temperature (^{o}C)

T_0 : Ambient/Blood Temperature (^{o}C)

ρ : Density (kg/m^3)

C_ρ : Specific heat capacity (J/kg ^{o}C)

k : Thermal conductivity (W/m ^{o}C)

b : Constant related to blood flow (W/m^3 ^{o}C)

q_m : Rate of metabolic heat generation (W/m^2)

At its core, the bioheat model is an energy balance equation. In this sense it will account for energy stored within the biological matter of interest, the energy lost and the net energy remaining. A positive net energy is synonymous with a rise in the temperature of the tissue of interest. Motivations for applying the bioheat equation in the context of microwave catheters and tissue ablation are numerous. They include the facts that with accurate modelling of heat flow mechanisms within the tissue/organ of interest heat losses due to the cooling effect blood flow has and heat rises due to the radiated fields by the catheter can be accounted for thereby allowing for the optimization of the treatment. It would allow for the prediction of the effects of various catheter designs. Finally, it would allow for and give rise to new strategies and designs through which ablation can be undertaken. Section 5.2. will address stability considerations associated with the practical formulation of the bioheat equation whilst Section 5.3. will attempt to outline how the bioheat equation can be used in the context of MW catheters and ablation.

5.2. *Stability Considerations*

In all numerical analysis, stability of the formulation is of the utmost importance. Numerical stability is regarded with setting an upper limit on the time increment or step. FDTD simulations is expected to satisfy the Courant condition while formulation related to the bioheat equation is expected to satisfy the Von Neumann stability condition [20]. It is worth mentioning that this stability condition relates, as one would expect, to the stability of linear partial differential equations on which finite differencing schemes have been applied. Its premise, hinges on Fourier decomposition of numerical errors. It is worth mentioning, that generally stability of all numerical schemes will be associated with the extent of error inherent in most schemes. In partial differential equations where there exists time dependence, an adequate stability condition will produce a solution that is bounded. Von Neumann's method has proven to be instrumental in maintaining the stability of the solution of the bioheat equation. The upper limit for the relevant time step should therefore be:

$$\delta_t \leq \frac{2\rho C_\rho \Delta^2}{12K + b\Delta^2} \tag{5.2}$$

where rather than having a time step expressed as a function of spatial increments Δ, the time step in the context of the bioheat equation is expressed as a function of the thermal properties of the medium in which the catheter is immersed as well the as the spatial increments of the FDTD simulation.

5.3.   *Application to Microwave Catheters*

While in its original format Pennes bioheat equation did not account for the heating effect of electromagnetic radiation it can be extended to include this effect through the introduction of SAR to it. As previously stated SAR is a term providing a measure of the amount of MW power that is absorbed by biological matter thereby accounting for the heating effect this power has. The bioheat equation now assumes the following form:

$$\rho C_\rho \frac{\partial T}{\partial t} = \nabla(k\nabla T) + \rho SAR - b(T - T_0) + q_m \tag{5.3}$$

This would now allow one to estimate heat rise in adjacent tissue due to the heating effect of the ablation process. The next step entails expressing the updated bioheat equation (5.3.1) in a cylindrical coordinate system. As previously stated, all formulation throughout this thesis follows a cylindrical coordinate system that utilizes the rotationally symmetric nature of the catheter. The bioheat equation now assumes the following form:

$$\frac{\partial T}{\partial t} = \frac{k}{\rho C_\rho}\left[\frac{\partial^2 T_r}{\partial r^2} + \frac{1}{r}\frac{\partial T_r}{\partial r} + \frac{\partial^2 T_z}{\partial z^2}\right] + \frac{1}{C_\rho}SAR - \frac{b}{\rho C_\rho}(T - T_0) \tag{5.4}$$

Note that the term relating to the rate of metabolic heat generation is dropped as its effects are negligible. The final step, is to apply the central difference theorem to (5.3.2) in order to discretize the equation thereby obtaining an equation which can be easily implemented in the numerical analysis.

This is shown as follows:

$$T^{n+1}(i, \text{j}) = T^n(i, \text{j}) + \frac{\Delta t \cdot k(i, j)}{\rho(i, j) \cdot C_\rho(i, j)} \frac{T_r^n(i+1, j) + T_r^n(i-1, j) - 2T_r^n(i, j)}{\Delta r^2}$$

$$+ \frac{\Delta t \cdot k(i, j)}{\rho(i, j) \cdot C_\rho(i, j)} \frac{1}{r(i, j)} \frac{T_r^n(i+1, j) + T_r^n(i, j)}{\Delta r}$$

$$+ \frac{\Delta t \cdot k(i, j)}{\rho(i, j) \cdot C_\rho(i, j)} \frac{T_z^n(i, j+1) + T_z^n(i, j-1) - 2T_z^n(i, j)}{\Delta z^2} \qquad (5.5)$$

$$+ \frac{\Delta t}{C_\rho(i, \text{j})} SAR(i, j) - \frac{\Delta t \cdot b(i, j)}{\rho(i, j) \cdot C_\rho(i, j)} (T^n(i, \text{j}) - T_0)$$

The result of temperature rise analysis is depicted in Fig. 37 below. Temperature continuously rises until it reaches a steady state value. At increasing radial separations from the catheter temperature rise seems to follow an exponential decay, synonymous with the decay of the field radiated by the catheter as radial separation increases.
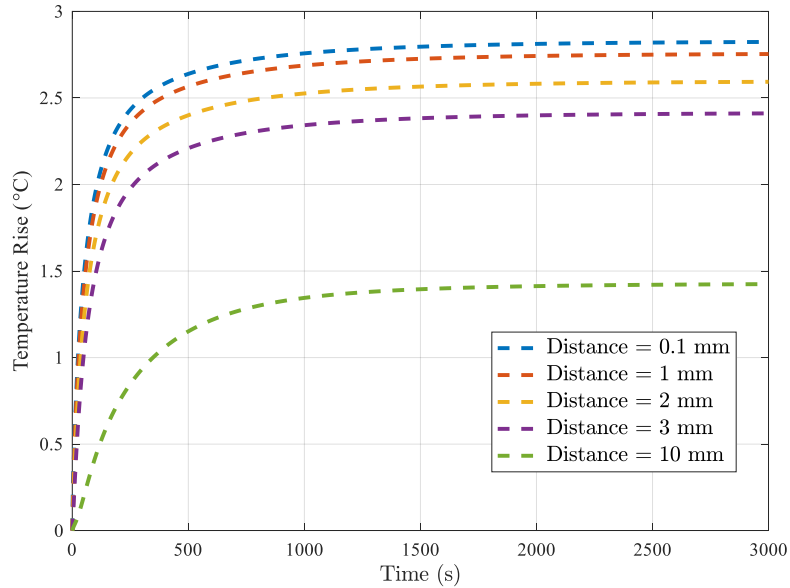

Fig. 37. Temperature rises obtained from the bioheat equation implementation

CHAPTER VI

CONCLUSIONS

A Finite Difference Time Domain study on the design of microwave catheters has been presented. Relevant design aspects, namely return loss and SAR distribution are calculated and presented.

It is shown that a simple dielectric coated monopole suffers from significant presence of surface waves and a resonant frequency of 5.3 GHz. It is later shown that to operate the catheter at the biological frequency of 2.45 GHz a terminating disk was highly effective at halving the monopole's resonant frequency.

Several structures are analyzed in order to eliminate the process of power coupling to leaky waves. The sleeve choke proved to be highly effective at doing so whilst attaining a satisfactory return loss of -14.61 dB at resonance. The second structure analyzed was the floating sleeve which only partially alleviated the issue of surface waves whilst achieving a return loss of -39.08 dB at resonance. The last of the relevant mechanisms was the internal match which also proved to be highly successful at eliminating said power whilst attaining a return loss of -49.39 dB at resonance. In short, the sleeve choke mechanism had three main benefits the first is the elimination of surface waves which lead to unwanted ablation of healthy tissue, the lowering of the resonant frequency to an optimal 2.45 GHz and thirdly reducing the possibility of hot spots as currents are eliminated within the choke.

The addition of a dielectric plug had a limited impact on resonant frequency and return loss but acted to improve fractional bandwidth and improve lateral SAR distribution. Furthermore, a dispersive FDTD algorithm in cylindrical co-ordinates for metamaterial design is presented. The effect of a metamaterial plug was the reduction of resonant frequency, allowing for catheter length reductions if for the application of interest, they are desirable. It also acted to guide and reinforce forward radiation from the catheter's terminating cap. Finally, the bioheat equation is integrated into the existing model. The relevant formulation, application of the central difference theorem along with the expression in cylindrical co-ordinates is presented. Analysis of temperature rises associated with the catheter insertion into a blood medium has been presented and discussed.

CHAPTER VII

FUTURE WORK

Microwave catheters have the potential of becoming a widely used therapeutic means of addressing tissue aberrancies, abnormal growths as well as cancer. Several areas of research can contribute towards furthering acceptance of this technology and gaining its wide scale implementation.

Investigation into other more compact structures that are capable of depositing larger amounts of power, whilst minimizing reflections, towards the end of the catheter and within affected tissue would prove instrumental in encouraging wide scale adoption of microwave catheters. Other means of eliminating surface waves would prove to be equally beneficial. Conducting experimental studies that would closely complement the results thereby encouraging physicians to adopt this technology is another area where future work should be focused. Finally, the fabrication and practical realization of novel materials as well as their interaction with biological matter ought to be investigated.

REFERENCES

[1] A. Taflove, *Computational electrodynamics*, 1st ed. Boston: Artech House, 1995.

[2] K. Shlager and J. Schneider, "A selective survey of the finite-difference time-domain literature", *IEEE Antennas and Propagation Magazine*, vol. 37, no. 4, pp. 39-57, 1995.

[3] T. Mackay and A. Lakhtakia, *Electromagnetic anisotropy and bianisotropy*, 1st ed. Hackensack, NJ: World Scientific Pub. Co., 2010.

[4] K. Pillai, J. Akhter, T. Chua, M. Shehata, N. Alzahrani, I. Al-Alem and D. Morris, "Heat sink effect on tumor ablation characteristics as observed in monopolar radiofrequency, bipolar radiofrequency, and microwave, using ex vivo calf liver model", *Medicine*, vol. 94, no. 9, p. 580, 2015.

[5] M. Lubner, C. Brace, J. Hinshaw and F. Lee, "Microwave tumor ablation: mechanism of action, clinical results, and devices", *Journal of Vascular and Interventional Radiology*, vol. 21, no. 8, pp. S192-S203, 2010.

[6] M. Kato, *Electromagnetics in biology*, 1st ed. Tokyo: Springer, 2006.

[7] World Health Organization (WHO), "Magnetic fields. Environmental health criteria", Geneva, 1987.

[8] J. Maloney, G. Smith and W. Scott, "Accurate computation of the radiation from simple antennas using the finite-difference time-domain method", *IEEE Transactions on Antennas and Propagation*, vol. 38, no. 7, pp. 1059-1068, 1990.

[9] R. Nevels, G. Arndt, G. Raffoul, J. Carl and A. Pacifico, "Microwave catheter design", *IEEE Transactions on Biomedical Engineering*, vol. 45, no. 7, pp. 885-890, 1998.

[10] H. Luyen, F. Gao, S. Hagness and N. Behdad, "High frequency microwave ablation for targeted minimally invasive cancer treatment", *The 8th European Conference on Antennas and Propagation (EuCAP 2014)*, 2014.

[11] H. T. Luyen, Y. Mohtashami, J. Sawicki, J. D. Shea, S. C. Hagness and N. Behdad, "Recent advances in designing balun-free interstitial antennas for minimally-invasive microwave ablation," *2015 International Symposium on Antennas and Propagation (ISAP)*, Hobart, TAS, 2015, pp. 1-4.

[12] R. Harrington, *Time-harmonic electromagnetic fields*, 1st ed. New York: IEEE Press, 2001.

[13] V. Veselago, "The electrodynamics of substances with simultaneously negative values of ε and μ", *Soviet Physics Uspekhi*, vol. 10, no. 4, pp. 509-514, 1968.

[14] B. Munk, *Metamaterials*, 1st ed. Hoboken, N.J.: John Wiley, 2009.

[15] J. Pendry, "Negative refraction makes a perfect lens", *Physical Review Letters*, vol. 85, no. 18, pp. 3966-3969, 2000.

[16] C. Sun and N. Sinitsyn, "Exact transition probabilities for a linear sweep through a Kramers-Kronig resonance", *Journal of Physics A: Mathematical and Theoretical*, vol. 48, no. 50, p. 505, 2015.

[17] Yan Zhao and Yang Hao, "Accurate modelling of the optical properties of left-handed media using a finite-difference time-domain method", *2007 IEEE Antennas and Propagation International Symposium*, 2007.

[18] R. Ziolkowski and E. Heyman, "Wave propagation in media having negative permittivity and permeability", *Physical Review*, vol. 64, no. 5, 2001.

[19] Y. Hao and R. Mittra, *FDTD modeling of metamaterials: theory and applications*, 1st ed. Artech House, 2009.

[20] Jianqing Wang and O. Fujiwara, "FDTD computation of temperature rise in the human head for portable telephones", *IEEE Transactions on Microwave Theory and Techniques*, vol. 47, no. 8, pp. 1528-1534, 1999.

[21] Y. Xuan and W. Roetzel, "Bioheat equation of the human thermal system", *Chemical Engineering & Technology*, vol. 20, no. 4, pp. 268-276, 1997.